



HAL
open science

Topology Optimization of Fluidic Pressure Loaded Structures using the Biot-Darcy Method

Godfred O. Agyekum, Laurent Cangémi, François Jouve

► **To cite this version:**

Godfred O. Agyekum, Laurent Cangémi, François Jouve. Topology Optimization of Fluidic Pressure Loaded Structures using the Biot-Darcy Method. 2022. hal-03809734v1

HAL Id: hal-03809734

<https://hal.science/hal-03809734v1>

Preprint submitted on 10 Oct 2022 (v1), last revised 25 Oct 2022 (v2)

HAL is a multi-disciplinary open access archive for the deposit and dissemination of scientific research documents, whether they are published or not. The documents may come from teaching and research institutions in France or abroad, or from public or private research centers.

L'archive ouverte pluridisciplinaire **HAL**, est destinée au dépôt et à la diffusion de documents scientifiques de niveau recherche, publiés ou non, émanant des établissements d'enseignement et de recherche français ou étrangers, des laboratoires publics ou privés.

Topology Optimization of Fluidic Pressure Loaded Structures using the Biot-Darcy Method

Godfred Oheneba Agyekum^{1*}, Laurent Cangémi^{1†}
and François Jouve^{2†}

^{1*}IFP Energies nouvelles, Rueil-Malmaison, 92852, France.

²Université Paris Cité, Laboratoire Jacques-Louis Lions (LJLL),
Paris, F-75006, France.

*Corresponding author(s). E-mail(s):

godfred.a.o.ezail@gmail.com;

Contributing authors: laurent.cangemi@ifpen.fr;

francois.jouve@u-paris.fr ;

†These authors contributed equally to this work.

Abstract

In many applications, design problems involving structures experience fluidic pressure loads. During topology optimization (TO) of such design problems, these loads adapt their direction and location with the evolution of the design, which poses various challenges. A novel approach to optimize a relaxed formulation of such design problems is presented to provide a continuous and consistent treatment of design-dependent pressure loads. Its effect is to allow for micro-perforated composite as admissible designs. The porosity of each finite element is related to its density variable using a regular function, yielding a smooth transition between the solid and void phases. A design-dependent pressure field is established using Biot-Darcy's law and the associated PDE is solved using the finite element method. The approach provides a computationally inexpensive evaluation of load sensitivities using the adjoint-variable method. Since it places no assumption on the number of holes cut within the domain, it can be seen as a topology optimization algorithm. Numerical results are presented for various two dimensional problems. We seek minimizers of the sum of the elastic compliance, fluid-elastic compliance and of the weight of a solid structure under fluidic pressure loads.

Keywords: Topology optimization, multi-scale, relaxed formulation, theory of homogenization, porous medium, adjoint methods, fluid-structure interaction.

1 Introduction

Shape optimization is a major issue in structural design and one of the most challenging aspects is what structural engineers refer to as layout or topology optimization. Its is nowadays well developed field with various methods and most have meanwhile attained a mature state. Moreover, their popularity as design tools for achieving solutions to a wide variety of problems involving single/multi-physics is growing consistently. Among these, design problems involving fluidic pressure loads pose several unique challenges: *(i)* identifying the structural boundary to apply such loads, *(ii)* determining the relationship between the fluidic pressure loads and the design variables, i.e., defining a design-dependent and continuous pressure field and *(iii)* efficient calculation of the fluidic pressure load sensitivities. Such problems can be encountered in the design of heat-exchangers [1–6], for various applications such as hot and cold fluids loaded and mechanical structures (e.g., combustion engines, air conditioning, power production or microturbines). Note that, the topology and performance of the optimized structures are directly related to the magnitude, location and direction of the fluidic pressure loads which vary with the design, for various applications such as hot and cold fluids loaded and mechanical structures (e.g., combustion engines, air conditioning, power production or microturbines). Note that, the topology and performance of the optimized structures are directly related to the magnitude, location and direction of the fluidic pressure loads which vary with the design.

In this paper, we target topology optimization to address the aforementioned challenges in the design of solid structures under fluid-pressure loads for a given weight of the solid. We carefully map the passage from the original optimization to its assumed relaxed formulation: allow a periodic distribution of holes of any shape and any size within the design region. The recipe is deceptive because the issue at stake is truly of a mathematical nature, the collection of admissible periodic holes should be such that meaningful optimality criteria can be proposed. A key problem characteristic is that the fluidic pressure loaded surface is not defined *a priori* but, it can be modified by the optimization process to (for instance) maximize stiffness. The main application of our work is the optimization of architected materials, also known as lattice materials which are becoming increasingly popular in the context of additive manufacturing. Below, we review the proposed topology optimization methods that involve pressure-loaded boundaries for structural designs.

In the case of topology optimization, Hammer and Olhoff [1] were first to propose design problems involving pressure loaded structures. Thereafter, several approaches have been proposed to apply and provide a proper treatment of

such loads in TO setting, which can be broadly classified into: (i) methods using boundary identification schemes [1, 7–11], (ii) level set method based approaches [6, 12–14], and (iii) approaches involving special methods, which avoid detecting the loading surface [15–19, 44].

Boundary identification techniques in general, are based on *a priori* chosen threshold density ρ_T : i.e., iso-density curves/surfaces are identified. Hammer and Olhoff [1] used the iso-density approach to identify the pressure loading facets Γ_{p_b} which they further interpolated via Bézier spline curves to apply the pressure loading. However, as per Du and Olhoff [7], this iso-density (isolines) method may furnish isoline-islands and/or separated isolines. Hence, valid loading facets may not be achieved. In addition, this method requires predefined starting and ending points for the exposed boundary Γ_{p_b} [1]. To circumvent this issue associated with the isolines method, Du and Olhoff [7] proposed a modified isolines technique. In [1, 7], the sensitivities of the pressure load are evaluated with respect to design variables using an efficient finite difference formulation. Lee and Martins [9] presented a method wherein one does not need to define starting and ending points *a priori*. In addition, they provided an analytical approach to calculate load sensitivities. However in [1, 7, 9], the sensitivities of the pressure loads, were confined to only those elements which are exposed to the pressure boundary loads Γ_{p_b} . One should refer to [8, 11] for methods evolving pressure loading boundary Γ_{p_b} . The methods presented in this paragraph do not account for load sensitivities within their topology optimization setting. Furthermore, as per Hammer and Olhoff [1], if the evolving pressure loaded boundary Γ_{p_b} coincides with the edges of the finite elements (FEs) then the load sensitivities with respect to design variables vanish or can be disregarded. Consequently, Γ_{p_b} no longer remains sensitive to infinitesimal alterations in the design variables unless the threshold value ρ_T is passed and thus, Γ_{p_b} jumps directly to the edges of a next set of FEs in the following topology optimization iteration. We emphasize that load sensitivities however may critically affect the optimal material layout of a given design problem, thus, considering load sensitivities in problems involving fluidic pressure loads is highly desirable. In addition, ideally these sensitivities should be straightforward to compute, implement and computationally inexpensive.

In contrast to density-based topology optimization, in the level-set-based approaches, an implicit boundary description is available that can be used to define the pressure load. On the other hand, being based on boundary motion, level-set methods tend to be more dependent on the initial design [6]. Gao et al. [12] (2004), employed a level set function (**LSF**) to represent the structural topology and overcame difficulties associated with the description of boundary curves in an efficient and robust way. Xia et al. [14] (2015), employed two zero-level sets of two **LSFs** to represent the free boundary and the pressure boundary separately. Wang et al. [20] (2016), employed the **Distance Regularized Level Set Evolution (DRLSE)** (see [13], 2010) to locate the structural boundary. They used the zero level contour of **LSF** to represent the loading boundary but did not regard load sensitivities. Recently, Feppon et

al. [6] (2018), employed a **Level Set Mesh Evolution (LSME)** to locate the structural boundary. They used Hadamard’s method of shape differentiation to solve a coupled thermal fluid-structure. Picelli et al. [21] (2019), proposed a method wherein Laplace’s equation is employed to compute hydrostatic fluid pressure fields, in combination with interface tracking based on a flood fill procedure. Shape sensitivities in conjunction with Ersatz material interpolation approach are used within their method.

Given how difficult is to identify a discrete boundary within density-based TO and obtain consistent sensitivity information, various researchers have employed special/alternative methods (without identifying pressure loading surfaces directly) to design structures experiencing pressure loading. Chen and Kikuchi [44] (2001), presented an approach based on applying a fictitious thermal loading to solve pressure loaded problems. Sigmund and Clausen [17] (2007), employed a mixed displacement-pressure formulation based finite element method in association with three-phase material (fluid/void/solid). Therein, an extra (compressible) void phase is introduced in the given design problem while limiting the volume fraction of the fluid phase and also, the mixed finite element methods have to fulfill the Babuška–Brezzi condition (BB-condition) which guarantees the stability of the element formulation [22]. Bourdin and Chambolle [15] (2003), also used three-phase material to solve such problems. Zheng et al. [11], (2009) introduced a pseudo electric potential to model evolving structural boundaries. In their approach, pressure loads were directly applied upon the edges of finite elements and thus, they did not account for load sensitivities. Additional physical fields or phases are typically introduced in these methods to handle the pressure loading. Recently, Kumar et al, [23] (2020), employed similar strategy based on Darcy’s law, to design both structures and compliant mechanisms loaded by design-dependent pressure loads using density-based TO. In addition, D. Hübner et al. [24] (2019), employed similar strategy based on Biot model derived by the homogenization of two decoupled problems: (1) deformation of a porous solid saturated by a slightly compressible static fluid and (2) Stokes flow through the rigid porous structure. The effective medium properties are given by the drained skeleton elasticity, the Biot stress coupling, the Biot compressibility coefficients, and by the hydraulic permeability of the Darcy flow model. Our method follows a similar strategy based on Biot-Darcy’s law to optimize a relaxed (or homogenized) formulation to provide a continuous and consistent treatment of design-dependent fluidic pressure loads, which has not been reported before. On one hand we carefully map the passage from the original shape optimization problem to its assumed relaxed formulation. This permits to introduce micro-perforated composite as admissible designs. Our motivation originates from the observation that many industrial applications in the field of energy involve multi-scale designs. For instance, heat exchangers feature periodic patterns visible at a microscopic scale which are geometrically modulated over larger scales. They are integrated into a suitable macroscopic structure so as

to maximize the exchange surface between hot and cold phases, while limiting the output pressure loss. We propose a new computational algorithm for two dimensional shape optimization that takes full advantage of a class of periodically perforated composite to design fluidic pressure loaded structures. The presented approach uses Biot-Darcy’s law and standard finite elements, for modeling and providing a suitable treatment of pressure loads. The Biot-Darcy’s law is adapted in a manner that the porosity of the FEs can be taken as design-dependent using a smooth function facilitating smoothness and differentiability. Consequently, prescribed pressure loads are transferred into a design dependent pressure field using a partial differential equation (PDE), which is further solved using the finite element method. The determined pressure field is used to evaluate consistent nodal forces using the finite element method. This two steps process offers a flexible and tunable method to apply the pressure loads and also, provides distributed load sensitivities, especially in the early stage of optimization. The latter is expected to enhance the exploratory characteristics of the TO process.

Regarding applications, most research on topology optimization involving fluidic pressure loads has thus far focused on compliance minimization problems and the present paper should be approached within such background. Several homogenized models exist depending on various scaling regimes assumed by the microstructure pattern (i.e., Darcy, Brinkman, or Stokes regimes, etc.) which makes it unclear which effective model should be used to describe a context featuring all possible regimes simultaneously at different locations in the domain. Thus, using the presented method, we not only design a rigorous pressure-loaded microstructures but also provide a suitable treatment of pressure loads, which suggests the novel potentiality of the method.

In Section 2, we carefully state the original shape optimization problem as well as its relaxed formulation. Next, in Section 3, we present the homogenized fluid-structure models using Biot-Darcy method. Then, in Section 4, we introduce the topology optimization problem formulation for fluidic pressure loaded structures and small-strains, and the associated sensitivity analysis. In Section 5, we present the TO process: it is an alternate direction algorithm, which successively computes the stress field through the solving of a coupled fluid-structure problem over the set of composites periodically perforated by hexagonal cells in 2-d. Finally, in Section 6, we present our numerical results: 2-d computations are displayed of various benchmark design problems involving fluid-pressure loaded structures and small deformation. As a final note, the following new aspects are presented:

- Biot-Darcy’s law is used to identify evolving pressure loading boundary which is performed by solving an associated **PDE**,
- the approach facilitates computationally inexpensive evaluation of the load sensitivities using the adjoint-variable method,
- the load sensitivities are derived analytically and consistently considered within the presented approach while synthesizing structures experiencing pressure loading,

- the method avoids explicit description of the pressure loading boundary (which proves cumbersome to extend to 3-d),
- the robustness and efficacy of the approach is demonstrated via various standard design problems related to structures,
- the method employs standard linear **FEs**, without the need for special **FE** formulations.

2 The original optimal design problem and its relaxed formulation

This section is essentially composed of reminders of existing results in homogenization based shape optimization of elastic structures. An adequate class of admissible designs is introduced which is precisely the concern of the theory of homogenization. The announced goal is to devise the least compliant structure compatible with the loads for a given weight of the structure, i.e.: to maximize the rigidity of an elastic structure under a weight constraint. We content ourselves to recall the main results detailed in [25], by Allaire, Bonnetier, Francfort and Jouve. These results will be useful for a good understanding of various related subjects that we will be discuss hereafter. The complete proof sometimes very technical can be found in [25].

Consider a bounded domain $\Omega \subset \mathbb{R}^N$ subject to "smooth enough" surface loadings f , e.g.: $f \in H^{-1/2}(\partial\Omega)^N$, satisfying a compatibility condition of equilibrium on the boundary $\partial\Omega$. Part of the domain is occupied by an isotropic linearly elastic material with elasticity:

$$A = \left(\kappa - \frac{2\mu}{N}\right)I_N \otimes I_N + 2\mu I_{2N}, \quad 0 < \kappa, \mu < +\infty, \quad (1)$$

while the remaining part of Ω is void. Let χ be the characteristic function of the part Ω_χ , occupied by the elastic material. Whenever Ω_χ is a smooth enough open subdomain of Ω , such that $\partial\Omega_\chi$ contains the part of $\partial\Omega$ where f is not zero, the elasticity problem in Ω_χ is well-posed, i.e., the following set of equations:

$$\begin{cases} \sigma = Ae(u) & e(u) = \frac{1}{2}(\nabla u + \nabla^t u), \\ \operatorname{div}(\sigma) = 0 & \text{in } \Omega_\chi, \\ \sigma \cdot n = f & \text{on } \partial\Omega_\chi \cap \partial\Omega, \\ \sigma \cdot n = 0 & \text{on } \partial\Omega_\chi \setminus \partial\Omega. \end{cases} \quad (2)$$

has a unique solution $u \in H^1(\Omega_\chi)^N$ (up to a rigid displacement field). Here u , is the displacement vector and σ is the associated Cauchy stress field uniquely defined in $L^2(\Omega_\chi; \mathbb{R}_s^{N^2})$. As such, σ can be extended to an element of $L^2(\Omega; \mathbb{R}_s^{N^2})$, which further realizes the minimum of the complementary energy over all statically admissible stress fields, i.e.:

$$c(\chi) := \int_{\Omega} A^{-1} \sigma \cdot \sigma \, dx = \min_{\tau \in \Sigma(\chi)} \int_{\Omega} A^{-1} \tau \cdot \tau \, dx, \quad (3)$$

where the set $\Sigma(\chi)$ is defined by:

$$\Sigma(\chi) = \left\{ \tau \in L^2(\Omega; \mathbb{R}_s^{N^2}) \mid \operatorname{div}(\tau) = 0 \text{ in } \Omega; \tau \cdot n = f \text{ on } \partial\Omega; \right. \\ \left. \tau(x) = 0 \text{ a.e. where } \chi(x) = 0 \right\} \quad (4)$$

The quantity $c(\chi)$, defined by (3), is called the compliance of the body and a straightforward integration by parts demonstrates that

$$c(\chi) = \int_{\partial\Omega} f \cdot u \, dx,$$

where u is the solution of the system (2). When $\chi(x)$, is the characteristic function of an arbitrary measurable subset of Ω (not necessarily open), the existence of σ is no longer guaranteed. A generalized compliance may however be defined as:

$$c(\chi) := \inf_{\tau \in \Sigma(\chi)} \int_{\Omega} A^{-1}\tau \cdot \tau \, dx, \quad (5)$$

with $\Sigma(\chi)$ is defined by (4) (note that, the infimum is not necessarily attained). The goal of the optimal design is devise the least compliant structure compatible with the loads for a given weight of the structure. Thus, the range of compliances $c(\chi)$ for all characteristic functions χ such that:

$$\int_{\Omega} \chi(x) \, dx = \Theta, \quad 0 < \Theta \leq |\Omega|,$$

is investigated and the optimal design reads as:

$$I := \inf \left\{ c(\chi) \mid \chi \in L^\infty(\Omega; \{0, 1\}); \int_{\Omega} \chi(x) \, dx = \Theta \right\}. \quad (6)$$

The optimal design problem defined in (6) is difficult to handle since it is constrained by:

$$\int_{\Omega} \chi(x) \, dx = \Theta. \quad (7)$$

Such a constraint is routinely handled in elementary calculus of variations through the introduction of a positive Lagrange multiplier. Thus, (6) is replaced by:

$$I(\ell) := \inf_{\chi \in L^\infty(\Omega; \{0, 1\})} \left\{ c(\chi) + \ell \int_{\Omega} \chi(x) \, dx \right\}, \quad (8)$$

in the hope that there exists a positive value ℓ for which the volume constraint (7) is met. That it is not so obvious in the case at hand, and as such it should be justified. We are unfortunately helpless in the matter as detailed in [25]. Thus, we content ourselves with the above unconstrained version of the original optimization problem.

Remark 1 For sake of simplicity, we consider only the case where surface loads are applied. A straightforward modification of the model would however permit the consideration of volume forces or the clamping of part of the boundary $\partial\Omega$, i.e.: the enforcement of a Dirichlet boundary condition $u = 0$. The reader is referred to the numerical examples presented in Sect. 6, which include different types of boundary conditions. The above optimization problem is usually referred to as a "single load" problem. This means that the elastic structure is optimized for a single configuration of loading forces and may well be totally inadequate for other loads. Its quite often more realistic to investigate "multiple loads" problem which amounts to an optimization of the structure for several configurations, i.e., various surface loadings f_1, \dots, f_p are given and we consider the minimization problem:

$$I_p(\ell) := \inf_{\chi \in L^\infty(\Omega; \{0,1\})} \left\{ \sum_{i=1}^p c_i(\chi) + \ell \int_{\Omega} \chi(x) \right\}, \quad (9)$$

where $c_i(\chi)$ is the generalized compliance defined by (5) for the boundary condition f_i .

It is well-known since the seminar counter-examples of Murat [26] that problems of the type (6) or (8) do not generally admit solution to the extent that minimizers do not exist among characteristic functions. The problem must be relaxed, i.e.: allow for micro-perforated composite as admissible designs and the optimum is achieved by a composite (or generalized) design. This is due to the fact that composite designs made of very small microstructures can always outperform genuine designs made of plain material. A composite design is described by the local density $\theta(x) \in L^\infty(\Omega; [0, 1])$ of material and an homogenized elasticity tensor $A^*(x)$ that depends on the microstructure at the point $x \in \Omega$. The homogenized or macroscopic displacement u^* of the structure is then solution of the following set of equations:

$$\begin{cases} \sigma = A^* e(u^*) & e(u^*) = \frac{1}{2}(\nabla u^* + \nabla^t u^*), \\ \operatorname{div}(\sigma) = 0 & \text{in } \Omega, \\ \sigma \cdot n = f & \text{on } \Gamma_N, \\ \sigma \cdot n = 0 & \text{on } \partial\Omega \setminus \Gamma_N, \end{cases} \quad (10)$$

such that Γ_N contains the part of $\partial\Omega$ where f is non zero. We emphasize that the problem is now defined on the whole working domain Ω and no longer on a design Ω_χ . Thus, the minimization problem (8) is replaced by:

$$I^*(\ell) := \min_{\tau \in \Sigma(\Omega)} \left\{ \min_{0 \leq \theta \leq 1} \left\{ c^*(\theta) + \ell \int_{\Omega} \theta \, dx \right\} \right\}, \quad (11)$$

where $\Sigma(\Omega)$ is defined by:

$$\Sigma(\Omega) = \left\{ \tau \in L^2(\Omega; \mathbb{R}_s^{N^2}) \mid \operatorname{div}(\tau) = 0 \text{ in } \Omega; \tau \cdot n = f \text{ on } \partial\Omega \right\}. \quad (12)$$

and $c^*(\theta)$ is defined by:

$$c^*(\theta) = \min_{A^*(x) \in G_{\theta(x)}} \int_{\Omega} A^{*-1} \tau \cdot \tau \, dx, \quad (13)$$

where $G_{\theta(x)}$ is the set of effective or homogenized Hooke's laws for microstructures of density $\theta(x)$. The quantity $c^*(\theta)$, defined by (13) is called the relaxed or homogenized compliance for a perforated composite material obtained by mixing the material A with holes in proportions $\theta(x)$ and $1-\theta(x)$. The main difficulties in the homogenized formulation (11) are first, to compute the relaxed compliance $c^*(\theta)$ (which may be different from the original compliance $c(\chi)$), second and the most important is to give a complete and explicit description of the set of admissible Hooke's laws G_{θ} . Unfortunately, the set of effective tensors resulting from the mixture in fixed volume fraction of two elastic materials is unknown for the general case of non-defined underlying microstructure topologies. This obstacle is alleviated in the particular case where the objective functional is the elastic compliance because its minimum can be computed among a well-known subset of the full set of effective tensors, namely that of a sequential laminates: see [25] for details. To circumvent these obstacles, following the lead of [27, 28], we propose to limit the set of admissible composite designs to microstructures for which the Hooke's law can be numerically computed (typically, periodic composites with hexagonal cells, e.g.: honeycomb cells).

For the remainder of this paper, we content ourselves with the relaxed version (11) of the original optimization problem (8). As such, we denote by u , the homogenized displacement solution of (10) and we seek minimizers for the optimal composite solution under fluidic pressure loads and with a given weight of an elastic material.

3 Fluid-structure model using Biot-Darcy approach

The material boundary of a given design domain Ω , evolves as the topology optimization (TO) progresses while forming an optimum material layout. Therefore, it is challenging especially in the initial stage of the optimization to locate an appropriate loading boundary Γ_{p_b} for applying the pressure loads. In addition, while designing especially fluidic pressure and small strain, establishing a design-dependent and continuous pressure field would aid to TO. From a fluid point of view, it was established in [29], that different regimes can exist within a foam-like composite. These regimes depend on the local Reynolds number evaluated using 3-d simulation of the pore-scale flow. It is shown that, a Darcy regime is established for Reynolds numbers lower than 0.3, while an inertia regime is established for a Reynolds greater than 30, preceded by a transition regime. The complexity of these real flow regimes is not taken into account in our present work and we consider in this first approach a flow of the

Darcean type. However, it was established in [29] that, a Darcy-Forchheimer type approach makes it possible to account for all possible regimes. Thus, exploring this sophisticated flow law is an obvious line of research for future work.

Here, Biot-Darcy's law is employed to establish the pressure field as a function of material density θ . Darcy's law defines the ability of a fluid to flow through porous media such as rock, soil or sandstone. It states that fluid flow through a unit area is directly proportional to the pressure drop per unit length ∇p and inversely proportional to the resistance of the porous medium to the flow μ ([30]). Mathematically,

$$\mathbf{q} := -\frac{\kappa_f}{\mu_f} \nabla p = -K^* \nabla p, \quad (14)$$

where \mathbf{q} , κ_f , μ_f , and ∇p represent the flux (ms^{-1}), permeability (m^2), fluid viscosity ($Nm^{-2}s$) and pressure gradient (Nm^{-3}), respectively. Further, K^{*1} ($m^4N^{-1}s^{-1}$) is termed as flow coefficient which expresses the ability of a fluid to flow through a porous medium. The flow coefficient is assumed to be related to the material density $\theta(x)$. In order to differentiate between void ($\theta(x) = 0$) and solid ($\theta(x) = 1$) phases of a finite element and at the same time ensuring a smooth and differentiable transition, $K^*(\theta(x))$ is modeled using a smooth function given by:

$$K^*(\theta(x)) := \min \left(\frac{\epsilon_0 + (1 - \epsilon_0)(1 - \theta(x))}{\theta(x)}, K_\infty \right), \quad (15)$$

where ϵ_0 , K_∞ are given thresholds, i.e., $\epsilon_0 = 10^{-4}$, $K_\infty = 10^3$, respectively. Our intent is to smoothly and continuously distribute the pressure drop over a certain penetration depth of the solid facing the pressure source: the validity of this assumption will be checked later in our numerical results in 4.2. In addition, the pressure field p is assumed to satisfy a Biot's law defined by:

$$p := Mm - Mbe_{vol}, \quad (16)$$

where M , m and e_{vol} are smooth enough functions related to the material density $\theta(x)$ given by

$$m(\theta(x)) := (1 - \theta(x))\rho, \quad M(\theta(x)) := \frac{1 - \theta(x)}{\kappa_v} \frac{b(\theta(x)) - (1 - \theta(x))}{\kappa_s}, \quad e_{vol} := \nabla \cdot u, \quad (17)$$

where ρ , κ_v , and κ_s represent the density of the flux², compressibility of the void and solid phase, respectively. The coefficient $e_{vol} = div(u)$, denotes a volume variation of the solid phase of proportion $\theta(x)$ at each finite element.

¹ $K^* = \frac{\kappa_f}{\mu}$ is termed "flow coefficient", noting the fact that this terminology is however sometimes used in literature with a different meaning.

²mass per unit volume of the fluid

The parameters M and b are the so called Biot modulus and Biot coefficient. The Biot's law (16) is assumed to be related to Darcy's law (14) by:

$$\mathbf{q} := mv_f = -K^*\nabla p, \quad (18)$$

where v_f represents the velocity (ms^{-1}) of the flux. Biot-Darcy's law renders a gradual pressure drop from the inner pressure boundary Γ_{pb} to the outer pressure boundary Γ_{po} : the validity of this assumption will be checked later in our numerical results in section 6. Consequently, equivalent nodal forces appear within the material as well as upon the associated boundaries. This penetrating pressure, originating because of Biot-Darcy's law, is a smeared-out version of an applied pressure load on a sharp boundary or interface³. We emphasize that, summing up the contributions of penetrating loads gives the resultant load. It is assumed that local differences in the load application have no significant effect on the global behaviour of the structure, in line with the Saint-Venant principle.

In addition to the Biot-Darcy equation (18), the equation of state using the law of conservation of mass in view of incompressible fluid is derived by:

$$\frac{\partial m}{\partial t} := -div(\mathbf{q}) = div(K^*\nabla p) \quad (19)$$

Consequently, we derived from the Biot's law (16), the equation:

$$\frac{\partial p}{\partial t} := M(\theta(x))\frac{\partial m}{\partial t} - M(\theta(x))b(\theta(x))\frac{\partial e_{vol}}{\partial t}, \quad (20)$$

Further to Biot-Darcy's law (18), we assume for sake of simplicity that our fluid model is continuous and stationary and that, the state equation satisfies the law of conservation of mass (in view of incompressible fluid) defined by:

$$\frac{\partial m}{\partial t} := -div(\mathbf{q}) = div(K^*\nabla p) = 0 \quad (21)$$

where in the particular case of a porous isotropic medium, the Biot's coefficient $b(\theta)$ is explicitly given by:

$$b(\theta(x)) := 1 - \frac{\kappa_s(\theta(x))}{\kappa}, \quad (22)$$

wherein, κ and $\kappa_s(\theta(x))$ represent the bulk moduli of the solid phase A and the effective (or homogenized) tensor $A^*(x)$. We emphasize that, $A^*(x)$ tends to A , when $\theta(x)$ tends to 1; thus, $\kappa_s(\theta)$ tends to κ . This formulation can effectively control the location and depth of penetration of the applied pressure. This paper should be approached within such background, i.e.: we assume that our fluid-structure model is defined in the particular case of a porous

³used in the approaches based on boundary identification

isotropic medium. In order to discuss the precise mathematical settings of our multiphysics system, we introduce the following spaces of functions defined by:

$$V(\Gamma_D^s) := \{v \in H^1(\Omega)^N \mid v = \mathbf{0}, \text{ on } \Gamma_D^s\}, \quad V(\Gamma_D^f) := \{q \in H^1(\Omega) \mid q = 0, \text{ on } \Gamma_D^f\}, \quad (23)$$

where Γ_D^s and Γ_D^f represent the homogeneous Dirichlet boundaries for the solid and fluid systems, respectively. We consider the subspace:

$$H^{1/2}(\Gamma_N^s) := \{v|_{\Gamma_N^s} \mid v \in V(\Gamma_D^s)\}, \quad (24)$$

and its dual space $H^{-1/2}(\Gamma_N^s)$. Using the Biot-Darcy's law (21), our fluid model is then defined by:

$$\text{(Biot-Darcy)} \quad \begin{cases} -\text{div}(K^* \nabla p) = 0 & \text{in } \Omega, \\ p = p_{in} & \text{on } \Gamma_D^f, \\ \mathbf{q}_\Gamma \cdot \mathbf{n} = f_f & \text{on } \Gamma_N^f, \\ \mathbf{q}_\Gamma \cdot \mathbf{n} = 0 & \text{on } \Gamma^f = \partial\Omega \setminus (\Gamma_D^f \cup \Gamma_N^f), \end{cases} \quad (25)$$

where $f_f \in H^{-1/2}(\Gamma_N^f)$ (satisfies a compatibility condition of equilibrium) is the enforcement of flux load on the part of its boundary Γ_N^f , i.e.: the enforcement of a Neumann boundary condition, and p_{in} is the loading pressure on the part of its boundary Γ_D^f , i.e.: the enforcement of a Dirichlet boundary condition. Thus, by a straightforward integration by parts, $p \in V(\Gamma_D^f)$ is the unique solution (up to a constant function) to the variational formulation defined by: $\forall q \in V(\Gamma_D^f)$

$$\int_{\Omega} K^*(\phi) \nabla p \cdot \nabla q \, dx - \int_{\Gamma_N^f} f_f q \, ds = 0 \quad (26)$$

where K^* is the homogenized permeability. Next, we weakly coupled the solution p of the fluid model (25) to the linear-elasticity problem defined by:

$$\text{(Biot-Coussy)} \quad \begin{cases} -\text{div}(\sigma) = -b \nabla p & \text{in } \Omega \\ \sigma \cdot \mathbf{n} = f_s & \text{on } \Gamma_N^s, \\ u = 0 & \text{on } \Gamma_D^s, \\ \sigma \cdot \mathbf{n} = 0 & \text{on } \Gamma^s = \partial\Omega \setminus (\Gamma_N^s \cup \Gamma_D^s), \\ \sigma = A^* \epsilon(u) & \epsilon(u) = \frac{1}{2}(\nabla u + \nabla^t u), \end{cases} \quad (27)$$

where $u \in V(\Gamma_D^s)$ is the unique solution (up to rigid displacement field). Here u is the homogenized displacement vector and σ is the associated Cauchy stress field. The vector function $f_s \in H^{-1/2}(\Gamma_N^s)$ is the body force applied on its boundary Γ_N^s , with a clamping of part on its boundary Γ_D^s . Wherein, the coupling is weak because the equations are solved consecutively, i.e.: first, the Biot-Darcy model, then the linear poro-elasticity model. Thus, by a

straightforward integration by parts, u is the unique solution to the variational formulation defined by: $\forall v \in V(\Gamma_D^s)$

$$\int_{\Omega} A^* e(u) \cdot e(v) dx - \int_{\Gamma_N^s} f_s v ds + \int_{\Omega} b \nabla p \cdot v dx = 0 \quad (28)$$

For the remainder of this paper, we weakly solve the variational formulations of the fluid-structure model equations.

4 Topology optimization problem formulation

Here, we follow topology optimization of modulated periodic microstructures using the homogenization method. A composite design is described by the local density $\theta(x)$ of the material and the homogenized tensor $A^*(x)$, that depends on the microstructure at the point $x \in \Omega$, in the design domain. We restrict ourselves to 2-d setting and restrain our analysis to a simple class of composites already used in [28], i.e., composites are periodically perforated by an hexagonal cell: a regular unit hexagon perforated by smooth hexagon hole, known as smooth honeycomb cell. This class of modulated periodic microstructures is known to be isotropic microstructures (or atleast very close to one): this assumption is numerically displayed on Fig. 3.

4.1 The Homogenized Hooke's laws

We denote by Y , the periodic smooth honeycomb cell. It is similar to the classical honeycomb cell, except that its interiors corners of its regular hexagon hole are rounded: see, Fig. 1(a). Consequently, when the density $\theta \in [0, 1]$ tends to one, its central smooth hexagon hole tends to a circle with a diameter going to zero. However, because of its rounded corners, the smooth honeycomb cell can not reach completely void, i.e.: θ going to zero is excluded. In addition, this smooth honeycomb is not parametrized using its density θ , for practical reason, but another parameter $h \in [0, 1]$, homogeneous to a distance. Indeed, in order to design this kind of cell, a parametric curve Γ_h depending on h is introduced and represents the boundary of its smooth central hole. We introduce some notations before giving its polar equation. Let $v(t) = (\cos(t), \sin(t))^T$ and n_i , with $i \in \{0, 1, 2\}$ represent the normal vectors of the three diagonals of $Y(h)$, defined by

$$n_0 = \begin{pmatrix} 0 \\ 1 \end{pmatrix}, \quad n_1 = \begin{pmatrix} \frac{\sqrt{3}}{2} \\ \frac{1}{2} \end{pmatrix}, \quad n_2 = \begin{pmatrix} \frac{\sqrt{3}}{2} \\ -\frac{1}{2} \end{pmatrix}. \quad (29)$$

Next, the polar equation of Γ_h is defined by:

$$r(t) = h \frac{\sqrt{3}}{2} \left(\sum_{i=0}^2 |v(t) \cdot n_i|^{k(h)} \right)^{\frac{-1}{k(h)}} \quad \text{with } t \in [0, 2\pi], \quad (30)$$

where k is positive coefficient, which depends on h . In this work, we took $k(h) = 4 + 20h^2$. We emphasize that h , is homogeneous to a distance and it is

similar to the parameter

$$m = \frac{\sqrt{3}}{2}(1 - \sqrt{1 - \theta}),$$

which denotes the relative width of bars with respect to the size of the periodic cell $Y(h)$.

Now, the polar equation of Γ_h relies on the following remarks and can be extended to other polygons. Let \mathcal{H} be a regular unit hexagon. By definition, \mathcal{H} is the set of all points such that, the maximal distance of a point in \mathcal{H} from the three diagonals is equal to $\frac{\sqrt{3}}{2}$. Let $M(r, t)$ be a point, with its polar coordinate denoted by (r, t) . Thus, M is a point in \mathcal{H} if and only if, its polar coordinate (r, t) satisfies

$$r \max_i |v(t) \cdot n_i| = \frac{\sqrt{3}}{2}. \quad (31)$$

Consequently, the polar equation of \mathcal{H} verifies

$$r(t) = \frac{\sqrt{3}}{2} (\max_i |v(t) \cdot n_i|)^{-1}. \quad (32)$$

In addition, we recall that

$$\left(\sum_{i=0}^2 |v(t) \cdot n_i|^k \right)^{\frac{-1}{k}} \xrightarrow{k \rightarrow \infty} \max_i |v(t) \cdot n_i|. \quad (33)$$

The polar equation of Γ_h comes from combining the polar equation of \mathcal{H} and the above limit. The parameter h is added in order to adjust the diameter of its inner hole. The interest of the smooth honeycomb relies on its smooth rounded corners, known to generate lower local concentration stress ([31, 32]), compare to the classical honeycomb.

The structure of the periodic cell Y as well as its Hooke's law are qualitatively similar to the celebrated Vigdergauz hexagonal cell [33], which is known to generate extreme composite microstructures, in the sense that they minimize the energy. Moreover, we do not claim that the smooth honeycomb can reach a particular elastic properties. The announced goal consists in reducing the stress concentration localized around the sharp corners of the classical honeycomb.

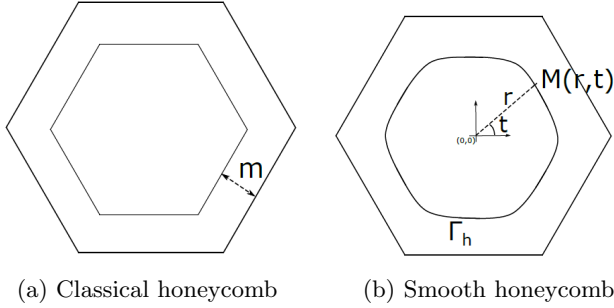


Fig. 1 Isotropic design cells (images taken from [28])

For sake of clarity, few important results on the theory of homogenization are recalled hereafter, the interested reader should refer to textbook [34], for details and explanations. Assume that, in a given macroscopic domain Ω , there is a periodic distribution of holes inside an elastic isotropic phase, with constant elastic tensor A . The periodicity size is denoted by $\epsilon > 0$, wherein the rescaled periodicity cell $Y(h)$ is the unit smooth honeycomb. Inside this unit periodic cell, the solid phase is the subset $Y_0(h)$, where its complement being the hole with boundary Γ_h ; see, Fig.1(b). Whenever ϵ tends to zero, the porous medium can be considered homogeneous, with an effective tensor $A^*(x)$. To compute the homogenized tensor A^* , one needs the so-called correctors w_{ij} , corresponding to the local displacements in the periodic cell $Y_0(h)$, defined for each pair $(i, j) \in \{1, 2\}$ as the solutions to the following set of equations defined by:

$$\begin{cases} \operatorname{div}(A(e_{ij} + e(w_{ij}))) = 0 & \text{in } Y_0 \\ A(e_{ij} + e(w_{ij})) \cdot \mathbf{n} = 0 & \text{on } \Gamma_h \\ y \mapsto w_{ij}(y) & Y_0 \text{ periodic,} \end{cases} \quad (34)$$

where $e_{ij} = \frac{1}{2}(e_i \otimes e_j + e_j \otimes e_i)$ is the basis of the symmetric tensors of order 2 and \mathbf{n} is the normal vector to the interior boundary Γ_h of $Y_0(h)$. Thus, the variational formulation associated to (34) is defined by: find $w_{ij} \in H_{\#}^1(Y_0, \mathbb{R}^2)$ such that

$$\forall \phi \in H_{\#}^1(Y_0, \mathbb{R}^2) \quad \int_{Y_0} A e(w_{ij}) : e(\phi) + \int_{Y_0} A e_{ij} : e(\phi) = 0, \quad (35)$$

which admits a unique solution (up to a rigid displacement field). The entries of the homogenized tensor $A^*(x)$ is then given in terms of the correctors w_{ij} , solutions of (35), defined by:

$$A_{ijkl}^* = \frac{1}{Y} \int_{Y_0} A(e_{ij} + e(w_{ij})) : (e_{kl} + e(w_{kl})) \, dy \quad \forall i, j, k, l \in \{1, 2\} \quad (36)$$

where the symbol $\#$ denotes the periodicity of the solutions w_{ij} . We emphasize that in (36), the coefficient is divided by the volume $Y(\mathbf{h})$. Generally, the volume $Y(\mathbf{h})$ is taken unitary in order to bypass this point. Restricting the analysis to periodic composites is an acceptable limitation, as the set Hooke's laws of periodic composites is dense in the set of all possible Hooke's laws reachable with composites [34]. However, restricting the set of periodic composites to regular hexagon cells with perforated smooth regular hexagon holes, i.e., smooth honeycomb, is clearly a loss of generality. Exploring a larger range of periodic microstructures is an obvious line of research for future work. Since the considered cell $Y(h)$ is specifically chosen in order to design an isotropic composites, only two coefficients of the homogenized tensor A^* (e.g., A_{1122}^* and A_{1212}^*) could be computed in order to fully characterize A^* . However, to confirm the isotropy of A^* , we computed all the its coefficients. Moreover, to demonstrate that the honeycomb cell $Y(h)$, is isotropic or at least very close to one, the range of θ is regularly discretized with 50 triangular elements. A linear material model with Young's modulus $\mathbf{E} = 12 \times 10^9 Nm^{-2}$ (i.e., 12GPa) and Poisson's ratio $\nu = 0.35$ were considered.

Remark 2 We emphasize that, the void (i.e., $\theta = 0$) is fill with a very compliant material, like in the SIMP method in order to avoid singularities of the effective tensor when the elasticity problem is solved; its elastic phase A_{min} is equal to ϵA , where herein, we took $\epsilon = 10^{-4}$.

We recall that, the homogenized tensor A^* is isotropic, thus, it is defined as:

$$A^* = 2\mu^* I_{2N} + \left(\kappa^* - \frac{2\mu^*}{N}\right) I_N \otimes I_N,$$

where κ^* and μ^* are the bulk and shear moduli of the homogenized Hooke's law A^* , with its Lamé coefficient defined by $\lambda^* = \kappa^* - \frac{2\mu^*}{N}$. Moreover, its entries are given by

$$\begin{cases} \mu^* = A_{ijij}^* \\ \lambda^* = A_{iijj}^* \\ \kappa^* = A_{iijj}^* + \frac{2}{N} A_{ijij}^* \end{cases} \quad \forall i, j \in \{1, \dots, N\} \quad (37)$$

The isotropy of the homogenized Hooke's law A^* implies some equalities between its coefficients, i.e.:

$$\forall i, j, k, l, p \in \{1, 2\} \quad \begin{cases} A_{iijk}^* = 0 \\ A_{iiii}^* = A_{jjjj}^* \\ A_{iijj}^* = A_{kkll}^* \\ A_{iiii}^* = A_{ijij}^* + A_{llpp}^* \end{cases} \quad (38)$$

Numerical results

Fig.2 depicts the relative errors to those equalities in (38), computed for discrete sample of material density θ : see, Fig.4. Furthermore, as it is known in [35] that any isotropic two-phase composite material is bounded by the Hashin-Shtrikman bounds, thus the homogenized bulk κ^* and shear μ^* moduli of A^* were also computed in order to confirm this assertion.

Remark 3 We recall that, the upper Hashin-Shtrikman bounds for the homogenized bulk κ_{HS} and shear μ_{HS} moduli are given by

$$\begin{cases} \kappa_{HS} = \frac{\kappa\mu\theta}{\kappa+\mu-\kappa\theta}, & \mu_{HS} = \frac{\kappa\mu\theta}{2(\kappa+\mu)-(\kappa+2\mu)\theta} & \text{in 2-D,} \\ \kappa_{HS} = \frac{4\kappa\mu\theta}{3\kappa+4\mu-3\kappa\theta}, & \mu_{HS} = \frac{(9\kappa+8\mu)\mu\theta}{5(3\kappa+4\mu)-6(\kappa+2\mu)\theta} & \text{in 3-D} \end{cases} \quad (39)$$

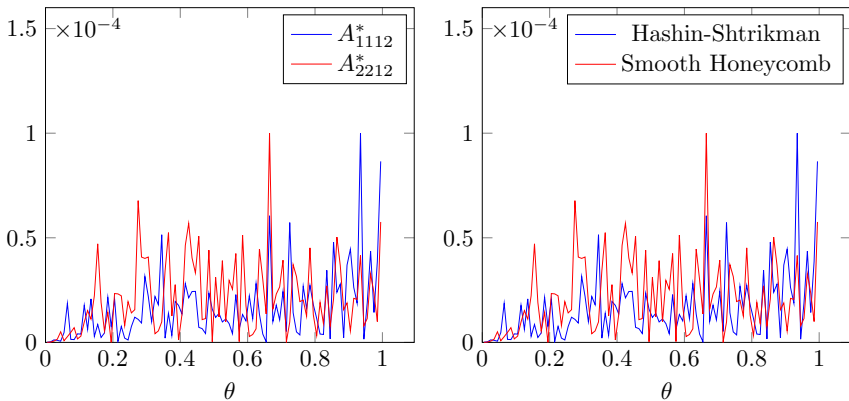


Fig. 2 Isotropy of the smooth honeycomb, i.e.: the maximum residual errors of equalities in 38

In each case, the coefficients are smooth increasing functions of the material density θ , which ensures that the optimization process will converge. We emphasize that, κ^* and μ^* are closed to the upper Hashin-Shtrikman bounds: see, Fig.3.

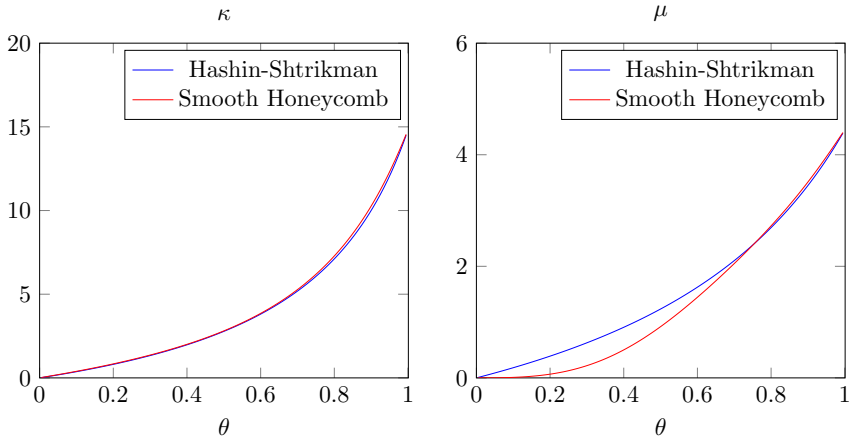


Fig. 3 The bulk κ^* (left) and shear μ^* (right) moduli of the smooth honeycomb wrt. Hashin-Shtrikman bounds

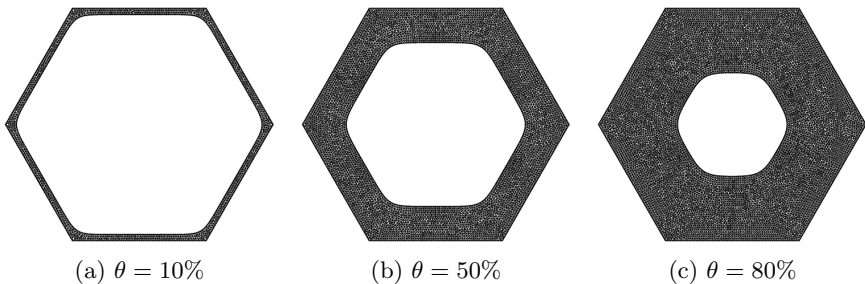


Fig. 4 The Smooth honeycomb cell for different values of to the density θ

4.2 The homogenized conductivity tensor

As in 4.1, starting from a microscopic description of a problem, one seeks a macroscopic or effective model problem in conductivity K^* , we introduce the so-called cell problems and since the considered cell Y is specifically chosen in order to design isotropic composites, only one of its coefficient (e.g., $(K^*)_{11}$) could be computed in order to fully characterized K^* , a scalar value. However to confirm the isotropy, we computed all its coefficients. We denote by $(e_i)_{i=1,2}$ the canonical basis of \mathbb{R}^2 . For each unit vector e_i , we consider the following conductivity problem in the periodic cell Y :

$$\begin{cases} -\operatorname{div}(K(e_i + \nabla w_i)) = 0 & \text{in } Y \\ y \mapsto w_i(y) & Y \text{ periodic,} \end{cases} \quad (40)$$

where $w_i(y)$ is the local variation of pressure created by an averaged (or macroscopic) gradient e_i . The homogenized conductivity tensor K^* is then given in terms of the correctors w_i , solutions of (40), defined by

$$(K^*)_{ij} = \frac{1}{Y} \int_Y K(e_i + \nabla w_i) : (e_j + \nabla w_j) dy \quad \forall i, j \in \{1, 2\} \quad (41)$$

The constant tensor K^* describes the effective or homogenized properties of the heterogeneous microstructure of periodic size ϵ . Likewise, note that K^* does not depend on the choice of domain Ω , source term f_f , or boundary condition on $\partial\Omega$.

Numerical results

The constant tensor K^* has been computed for the hexagonal cells in 2-d, on the same scheme as the homogenized tensor $A^*(\theta)$ for different values of the density. Figure 5 displays the homogenized flow coefficient K^* computed for a discrete values of the density with respect to the hexagonal cell and normalized smooth function given by (15). As expected, K^* is a decreasing function with respect to the density θ . It is noted that the residual $|(K^*)_{11} - (K^*)_{22}| \leq 10^{-6}$ and $(K^*)_{12} \leq 10^{-3}$, for the hexagonal cell, which validates the isotropy. We emphasize that the flow coefficient K^* can be approximated by the normalized smooth function, that is defined by (15).

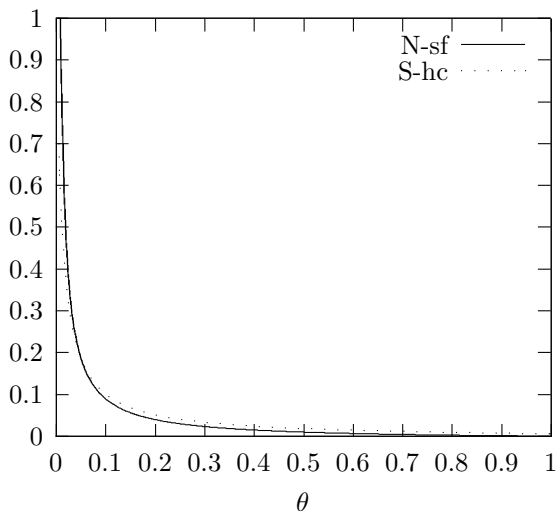


Fig. 5 The homogenized flow coefficient history wrt. the Smooth honeycomb (S-hc) and normalized smooth function (N-sf) in (15)

5 Sensitivity analysis

Here, we present the optimization problem formulation associated to fluidic-pressure loaded structures and discuss the sensitivity analysis for such design problems. The standard formulation, namely the minimization of compliance is considered to design pressure loaded stiff structures, where the optimization problem is given by the constrained formulation:

$$\min_{\substack{0 \leq \theta \leq 1 \\ \frac{1}{|\Omega|} \int_{\Omega} \theta \, dx = \Theta}} c^*(\theta) \quad (42)$$

where $c^*(\theta)$ is the relaxed objective function defined by:

$$c^*(\theta) := \int_{\Gamma_N} f_s \cdot u \, ds + \int_{\Omega} (-b \nabla p) \cdot u \, dx = \min_{\tau \in H_0} \left\{ \min_{A^*(x) \in G_{\theta}} \int_{\Omega} A^{*-1} \tau \cdot \tau \, dx \right\}, \quad (43)$$

with H_0 defined by

$$H_0 = \left\{ \tau \in L^2(\Omega; \mathcal{M}_2^s) \mid \begin{cases} -\operatorname{div}(\tau - b p I_2) = 0 & \text{in } \Omega \\ \tau \cdot n = f_s & \text{on } \Gamma_N^s \\ \tau \cdot n = 0 & \text{on } \Gamma^s \end{cases} \right\} \quad (44)$$

wherein, $\Gamma^s = \partial\Omega \setminus \Gamma_N^s$ is the free part of boundary $\partial\Omega$. We recall that, we only explicitly compute the optimization process on a subset of all possible Hooke's laws G_{θ} , i.e.: composites periodically perforated by smooth honeycomb cell. Therefore, the set of effective elasticity tensors $\{A^*(\theta) \mid \theta \in L^{\infty}(\Omega, [0, 1])\}$ has to be characterized. The proposed strategy consists in computing the material properties for a discrete sample of parameter values and using the collected data to construct a surrogate model for the constitutive law (by a simple linear interpolation). Next, the optimization problem (42) is recast as follow:

$$\min_{\theta} c^*(\theta) = \min_{\theta} \int_{\Omega} A^*(\theta) e(u) : e(u) \, dx, \quad (45)$$

where u is the unique solution to the coupled fluid-elasticity problem given by

$$\begin{cases} (i) & -\operatorname{div}(K \nabla p) = 0 \\ (ii) & -\operatorname{div}(A^* e(u)) = -b \nabla p \\ (iii) & \frac{1}{|\Omega|} \int_{\Omega} \theta \, dx = \Theta \end{cases} \quad (46)$$

where Θ is the prescribed volume fraction. Note that, all mechanical equilibrium equations are satisfied under small strain assumption. The optimization problem is then solved using the alternate minimization algorithm [34], which consists in minimizing successively the stress tensor through the solving of the coupled fluid-elasticity problem and then the density θ through a projected

gradient method: it is an algorithm based on *optimality criteria*. We emphasize that, the boundary value problems in (46) are solved in each iteration in combination with the respective boundary conditions.

In a gradient-based topology optimization, it is essential to determine sensitivities of the objective functional and the constraints with respect to the design variable(s). In general, the formulated objective functional depends upon both the state variable u , solution to the mechanical equilibrium equations and the design variable(s). In order to discuss the precise mathematical settings, we introduce the following set of admissible design variables \mathcal{U}_{ad} , defined by

$$\mathcal{U}_{ad} := \left\{ \theta(x) \in L^\infty(\Omega) \mid \theta(x) \in [0, 1], \forall x \in \Omega \right\} \quad (47)$$

We define the applications $\theta \rightarrow u(\theta)$, $\theta \rightarrow p(\theta)$, where $\theta \in \mathcal{U}_{ad}$ is associated to the solution $\{u(\theta), p(\theta)\} \in V(\Gamma_D^s) \times V(\Gamma_D^f)$ of the state equations (under volume constraints):

$$\begin{cases} (i) & -\operatorname{div}(K(\theta)\nabla p) = 0 \\ (ii) & -\operatorname{div}(A^*(\theta)e(u)) = -b\nabla p \\ (iii) & \frac{1}{|\Omega|} \int_\Omega \theta \, dx = \Theta \end{cases} \quad (48)$$

As already known [36], the above maps are continuous and differentiable in \mathcal{U}_{ad} , where the directional derivative at θ of $u(\theta)$ and $p(\theta)$ with respect to $\bar{\theta} \in L^\infty(\Omega)$ are defined respectively by:

$$\langle p'(\theta), \bar{\theta} \rangle = \bar{p}, \quad \langle u'(\theta), \bar{\theta} \rangle = \bar{u}, \quad (49)$$

where $\bar{p} \in H_0^1(\Omega)$ and $\bar{u} \in H_0^1(\Omega)^2$ are the unique solutions (up to constant functions) to the system given by:

$$\begin{cases} (i) & -\operatorname{div}(K(\theta)\nabla \bar{p}) = \operatorname{div}(\bar{K}\nabla p) \\ (ii) & -\operatorname{div}(A^*(\theta)e(\bar{u})) = \operatorname{div}(\bar{A}^*e(u)) - \bar{b}\nabla p - b\nabla \bar{p}, \end{cases} \quad (50)$$

where

$$\bar{K} = \langle K'(\theta), \bar{\theta} \rangle, \quad \bar{A}^* = \langle (A^*)'(\theta), \bar{\theta} \rangle \quad \text{and} \quad \bar{b} = \langle b'(\theta), \bar{\theta} \rangle \quad (51)$$

represent the directional derivatives at θ with respect to $\bar{\theta}$.

Proof Here, we only give the main results, the reader is referred to [36] for a complete proof. Let $(\theta, \bar{\theta}) \in \mathcal{U}_{ad} \times L^\infty(\Omega)$. For all $t > 0$ small enough, $\hat{\theta}(t) = \theta + t\bar{\theta}$ belongs to \mathcal{U}_{ad} . Thus, $\hat{p}(t) = p(\hat{\theta}(t))$ and $\hat{u}(t) = u(\hat{\theta}(t))$ are solutions to the system given by:

$$\begin{cases} (i) & -\operatorname{div}(\hat{K}(t)\nabla \hat{p}(t)) = 0 \\ (ii) & -\operatorname{div}(\hat{A}^*(t)e(\hat{u}(t))) = -\hat{b}(t)\nabla \hat{p}(t) \end{cases} \quad (52)$$

where,

$$\hat{K}(t) = K(\hat{\theta}(t)), \quad \hat{A}^*(t) = A^*(\hat{\theta}(t))$$

We then derive the system (52) with respect to the variable t and the resulting derivatives are evaluated at $t = 0$ in order to get the obtained system (50). \square

As already known [36], the objective functional given by:

$$c^*(\theta) = \int_{\Gamma_N} f_s \cdot u \, ds + \int_{\Omega} (-b\nabla p) \cdot u \, dx = \int_{\Gamma_N} j_1(u) \, ds + \int_{\Omega} j_2(u, p) \, dx \quad (53)$$

is differentiable and the directional derivative at θ with respect to $\bar{\theta}$ is given by:

$$\langle c'^*(\theta), \bar{\theta} \rangle = \int_{\Gamma_N} j'_1(u) \bar{u} \, ds + \int_{\Omega} \frac{\partial j_2}{\partial u}(u, p) \bar{u} \, dx + \int_{\Omega} \frac{\partial j_2}{\partial p}(u, p) \bar{p} \, dx \quad (54)$$

wherein, $\bar{p} \in H_0^1(\Omega)$ and $\bar{u} \in H_0^1(\Omega)^2$ are the unique solutions to the equations (50), respectively. Unfortunately, equation (54) is **unusable in practice**, because we cannot deduce a simple expression of the derivative $c'^*(\theta)$. Indeed, \bar{u} and \bar{p} are linear functions with respect to $\bar{\theta}$, which are non-explicit. To circumvent this issue, the presented Biot-Darcy-based TO method facilitates use of adjoint-variable method to determine the sensitivities, which is performed using the C ea method.

We introduced the Lagrange multiplier for the constraints (48), associating $\{p(\theta), u(\theta)\}$ to θ , which is $\{\underline{p}, \underline{u}, \ell\} \in H_0^1(\Omega) \times H_0^1(\Omega)^2 \times \mathbb{R}^{**}$, where ℓ is the Lagrange multiplier designed to respect the volume constraint. In addition, an augmented performance function known as the Lagrangian \mathcal{L} can be defined using the objective function and the mechanical state equations defined by:

$$\begin{aligned} \mathcal{L}(\hat{\theta}, \hat{u}, \hat{\underline{u}}, \hat{p}, \hat{\underline{p}}, \ell) &:= c^*(\hat{\theta}) + \int_{\Omega} \hat{\underline{u}}(-\text{div}(A^*(\hat{\theta})e(\hat{u})) + b(\hat{\theta})\nabla\hat{p}) \, dx \\ &+ \int_{\Omega} \hat{\underline{p}}(-\text{div}(K^*(\hat{\theta})\nabla\hat{p})) \, dx + \ell(\int_{\Omega} \hat{\theta} \, dx - \Theta), \end{aligned} \quad (55)$$

wherein, $(\hat{\theta}, \hat{u}, \hat{\underline{u}}, \hat{p}, \hat{\underline{p}}) \in L^\infty(\Omega) \times H_0^1(\Omega; \mathbb{R}^2)^2 \times H_0^1(\Omega; \mathbb{R})^2$ are independent variables. We emphasize that the compliance $c^*(\hat{\theta})$ depends upon the state variables u and p . By straightforward integration by parts, we get

$$\begin{aligned} \mathcal{L}(\hat{\theta}, \hat{u}, \hat{\underline{u}}, \hat{p}, \hat{\underline{p}}, \ell) &:= c^*(\hat{\theta}) + \int_{\Omega} (A^*(\hat{\theta})e(\hat{u}) : e(\hat{\underline{u}}) + b(\hat{\theta})\nabla\hat{p} \cdot \hat{\underline{u}}) \, dx \\ &+ \int_{\Omega} K^*\nabla\hat{p} \cdot \nabla\hat{\underline{p}} \, dx + \ell(\int_{\Omega} \hat{\theta} \, dx - \Theta), \end{aligned} \quad (56)$$

Next, the sensitivities are evaluated by differentiating (56) with respect to u and p in directions $\phi_u \in H^1(\Omega)^2$ and $\phi_p \in H^1(\Omega)$ defined by:

$$\left\langle \frac{\partial \mathcal{L}}{\partial u}(\hat{\theta}, \hat{u}, \hat{\underline{u}}, \hat{p}, \hat{\underline{p}}, \ell), \phi_u \right\rangle = - \int_{\Omega} b(\hat{\theta}) \nabla p \cdot \phi_u + \int_{\Omega} A^*(\hat{\theta}) e(\phi_u) : e(\hat{\underline{u}}) dx \quad (57)$$

and

$$\left\langle \frac{\partial \mathcal{L}}{\partial p}(\hat{\theta}, \dots), \phi_p \right\rangle = \int_{\Omega} (-b \nabla \phi_p) \cdot u dx + \int_{\Omega} b(\hat{\theta}) \nabla \phi_p \cdot \hat{\underline{u}} + \int_{\Omega} K^* \nabla \phi_p \cdot \nabla \hat{\underline{p}} dx \quad (58)$$

which when it vanishes, is nothing more than the variational formulation associated to adjoint-state. Furthermore, the derivatives with respect \underline{u} and \underline{p} in directions $\phi_u \in H^1(\Omega)^2$ and $\phi_p \in H^1(\Omega)$ are simply the state equations defined by:

$$\left\langle \frac{\partial \mathcal{L}}{\partial \underline{u}}(\hat{\theta}, \hat{u}, \hat{\underline{u}}, \hat{p}, \hat{\underline{p}}, \ell), \phi_u \right\rangle = \int_{\Omega} \left(A^* e(\hat{\underline{u}}) : e(\phi_u) dx + b \nabla \hat{p} \cdot \phi_u \right), \quad (59)$$

and

$$\left\langle \frac{\partial \mathcal{L}}{\partial \underline{p}}(\hat{\theta}, \hat{u}, \hat{\underline{u}}, \hat{p}, \hat{\underline{p}}, \ell), \phi_p \right\rangle = \int_{\Omega} K^* \nabla \hat{p} \cdot \nabla \phi_p dx, \quad (60)$$

which when it vanishes, is nothing more than the variational formulation associated to state equations (48). Finally, the partial derivative of the Lagrangian \mathcal{L} with respect to θ in direction $\bar{\theta} \in L^\infty(\Omega; \mathbb{R})$ at the stationary point $(u, \underline{u}, p, \underline{p})$ is defined by:

$$\left\langle \frac{d\mathcal{L}}{d\theta}, \bar{\theta} \right\rangle = \int_{\Omega} \left(-e(u)^T \frac{\partial A^*}{\partial \theta} e(u) + \underbrace{\left(e(u)^T \frac{\partial A^*}{\partial \theta} e(u) + \frac{\partial K^*}{\partial \theta} \nabla p \cdot \nabla \underline{p} + \frac{\partial b}{\partial \theta} \nabla p \cdot \underline{u} + \ell \right)}_{\text{Load sensitivities}} \right) \bar{\theta} dx \quad (61)$$

6 Topology optimization over composite materials

6.1 Alternate minimization method

This section presents the proposed numerical algorithm, which is based on the homogenization method. The key idea is to compute composite designs for the relaxed formulation rather than "classical" designs, which are merely approximately optimal for the original formulation. Our optimization problem is solved using the alternative minimization algorithm. We seek minimizers of sum of the elastic compliance, fluid-elastic compliance and of the weight of a solid structure under fluidic pressure loads.

6.1.1 Minimizing over the stress field.

Minimization over the stress field σ consists in solving the linear elasticity problem (27) over the effective tensor $A^*(x)$, for given design $\theta(x)$ of microstructure periodically perforated by the smooth honeycomb cell. Consequently, the linear elasticity problem (27) can be recast as a variational problem defined by:

$$v \in V(\Gamma_D^s), \quad \int_{\Omega} A^*(\theta)e(u) : e(v) dx = \int_{\Gamma_N^s} f_s \cdot v ds + \int_{\Omega} (-b\nabla p) \cdot v dx \quad (62)$$

which numerically is solved using P_1 finite elements to compute the displacement vector field u .

6.1.2 Minimizing over the density field.

Minimization over the density field θ for a given stress tensor σ is performed using the projected gradient algorithm. The minimum compliance problem defined by (43) is not a self-adjoint, hence one needs to define the associated adjoint problem, which we define herein using the C ea method presented in sect.(5). The descend direction $h = d\theta$ is given by solving the bilinear equation:

$$\left\langle \frac{\partial \mathcal{L}}{\partial \theta}, h \right\rangle = - \int_{\Omega} \left(e(u)^T \frac{\partial A^*}{\partial \theta} e(u) - \underbrace{\left(e(u)^T \frac{\partial A^*}{\partial \theta} e(\underline{u}) + \frac{\partial K^*}{\partial \theta} \nabla p \cdot \nabla \underline{p} + \frac{\partial b}{\partial \theta} (\theta) \nabla p \cdot \underline{u} + \ell \right)}_{\text{Load sensitivities}} \right) h dx, \quad (63)$$

where the descend direction $h = d\theta$, has to satisfy the inequality given by:

$$\left\langle \frac{\partial \mathcal{L}}{\partial \theta}(\theta, u, \underline{u}, p, \underline{p}, \ell), d\theta \right\rangle < 0 \quad (64)$$

which is achieved by choosing:

$$d\theta = \left(-e(u)^T \frac{\partial A^*}{\partial \theta} e(u) + \underbrace{\left(e(u)^T \frac{\partial A^*}{\partial \theta} e(\underline{u}) + \frac{\partial K^*}{\partial \theta} \nabla p \cdot \nabla \underline{p} + \frac{\partial b}{\partial \theta}(\theta) \nabla p \cdot \underline{u} + \ell \right)}_{\text{Load sensitivities}} \right) \quad (65)$$

At iteration n , the optimal density θ is then updated by performing the projected gradient:

$$\theta^{n+1} = P_{[0,1]}(\theta^n + \delta d\theta), \quad (66)$$

where $\delta > 0$ is the step size and $P_{[0,1]}$ is the projection operator on the interval $[0, 1]$. The value of the Lagrange multiplier ℓ is computed at each iteration by a dichotomy process designed to respect the volume constraint. We emphasize that the exact value of ℓ can not be analytically given because of the projection operator: numerically, the partial derivative of the Lagrangian $\frac{\partial \mathcal{L}}{\partial \theta}$ is regularized using an equivalent H^1 -norm by solving the following variational formulation:

$$\int_{\Omega} \left(\frac{\partial \mathcal{L}}{\partial \theta} h + \eta^2 \nabla \frac{\partial \mathcal{L}}{\partial \theta} \cdot \nabla h \right) dx = - \int_{\Omega} \left(\frac{\partial A^*}{\partial \theta} e(u) : e(u) - \frac{\partial A^*}{\partial \theta} e(u) : e(\underline{u}) - \frac{\partial K^*}{\partial \theta} \nabla p \cdot \nabla \underline{p} - \frac{\partial b}{\partial \theta} \nabla p \cdot \underline{u} - \ell \right) h dx, \quad (67)$$

where η is a small coefficient, which typically depends on the size of the elements of the mesh: thanks to this coefficient, we are able to numerically regularize the partial derivative on a length scale of order η and to limit the checkerboard effect on the density θ , similar to those reported in [37–39]. In practice, we use an adaptive step size δ , which consists in increasing δ by 20%, if the newly computed homogenized structure is accepted: if current compliance is lower than the previous one, else δ is divided by 2.

6.1.3 Volume constraint.

As explained in sect. 2, we do not know how to determine ℓ beforehand. As such, an alternative computations were performed, where the Lagrange multiplier ℓ is adjusted at each iteration, so that the corresponding value of the optimal density satisfies the volume constraint. In other words, once the stress σ^n is computed through (62), we determine θ^n through (66) and then ℓ^n is determined through a simple iterative procedure, namely by dichotomy.

6.2 Implementation

This section presents our complete optimization process to perform topology optimization of structures under fluidic pressure loads and some general difficulties related to the homogenization method.

6.2.1 Complete optimization algorithm.

The Alternate direction algorithm is an iterative method, structured as follows:

Algorithm 1

1. Initialization of the design variable θ such that :

$$\forall x \in \Omega \quad \theta^0(x) = \frac{\Theta}{\int_{\Omega} 1 \, dx}$$

2. Iteration until convergence, for $n \geq 0$:
 - (a) Computation of the state variable p^n through the Biot-Darcy problem (25), with design variable $(\theta^n(x), A^*(x))$
 - (b) Computation of the stress tensor σ^n through the linear elasticity problem (27), with design shape $(\theta^n(x), A^*(x))$
 - (c) Computation of the descend direction $d\theta^n$ for the stress tensor σ^n using formulas (64-67)
 - (d) Updating the design variable θ^{n+1} using formulas (65) for the descend direction $d\theta^n$ and then updating the effective tensor $(\theta^{n+1}(x), A^*(x))$, by linear interpolation.
-

Note that, the alternate direction algorithm is appared to the two known methods in [40–42].

6.2.2 Convergence criterion.

The procedure is iterated until the quantity

$$\max \left(\left(\max_i (|\theta_i^{n+1} - \theta_i^n|), 1 - \frac{\int_{\Omega} A^{*-1}(\theta^{n+1})\sigma^{n+1} : \sigma^{n+1} \, dx + \ell \int_{\Omega} \theta^{n+1} \, dx}{\int_{\Omega} A^{*-1}(\theta^n)\sigma^n : \sigma^n \, dx + \ell \int_{\Omega} \theta^n \, dx} \right) \right)$$

becomes smaller than a preset threshold. About 100 iterations are required to reach a criterion of order 10^{-5} . Other convergence criteria could be used, for instance the L^2 norm of $\sigma^{n+1} - \sigma^n$.

7 Numerical results and discussion

To demonstrate that evaluation of the consistent nodal loads seen in sect.3 from the obtained pressure field produces physically correct results, various (benchmark) design problems involving fluidic pressure loaded stiff structures and small strains are solved to show the efficacy and robustness of the proposed method, while minimizing the sum of the elastic compliance, fluid-elastic compliance and of the weight of a solid structure. Any change in the value of

considered parameters is reported within the definition of the problem formulation. The above algorithm has been implemented in FreeFem++[43], where all the unknowns are discretized using P_1 finite elements. For all our computations, a linear material model with Young's modulus $\mathbf{E} = 12 \times 10^9 Nm^{-2}$ and Poisson's ratio $\nu = 0.35$ are considered. The void (i.e., $\theta = 0$) is replaced with a very compliant material: namely, the smallest admissible value of θ is fixed at $1.e - 3$, in order to avoid singularities of the effective tensor when the elasticity problem is solved.

7.1 Pressurized arch

This example was originally introduced and solved in [11, 23]. A structure with dimensions $0.2m \times 0.1m$ is fixed at the edges of its left and right bottom on a zone of width $\frac{1}{8}$, while a pressure load $p = 1$ bar (i.e., $1 \times 10^5 Nm^{-2}$) is applied to the bottom and vanishes on the boundary $\Gamma_{p_0}^f$ (i.e., $p|_{\Gamma_{p_0}^f} = 0$): see Fig.6 for a schematic of this test case. The workspace Ω is discretized with 44492 triangular elements. Evidently, prior to the analysis, the force contribution from the prescribed pressure appears only in y -direction.

On Fig.7, we plot the objective function history for this calculation: smooth and relatively fast convergence is observed; while Fig.8 displays the output of the alternate minimization algorithm for a volume fraction set to $\Theta = 20\%$, with the resulting pressure field, deformed mesh, and von Mises stress at the final state. The density θ is represented with a gray scale: areas where $\theta = 1$ are black (pure material), whereas white regions correspond to voids.

The topology of the result is similar to that obtained in previous literature [23], for similar problems with different design and optimization settings. Although one can guess a "shape" on the edges of the structure, its center contains a large composite zone.

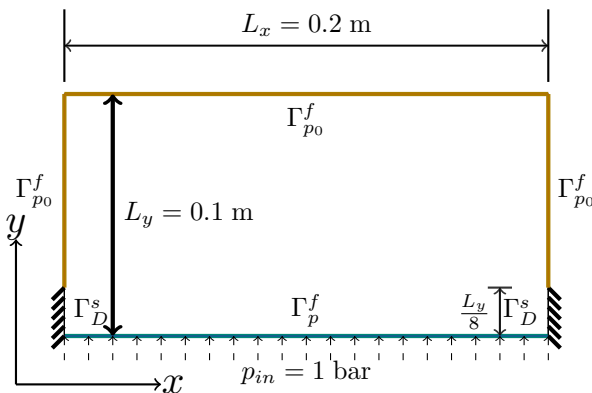


Fig. 6 Setting for fluid-elastic compliance minimization problem of 7.1 issued from [11, 23]

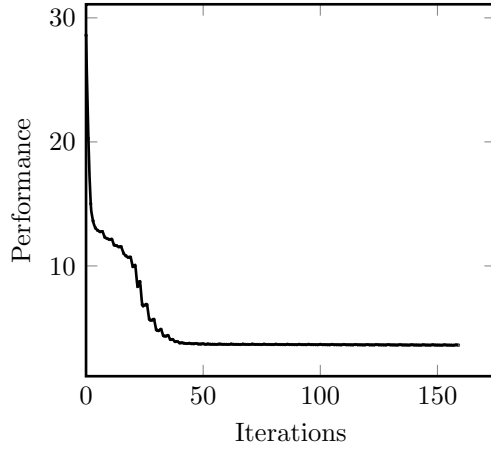


Fig. 7 Convergence history for fluid-elastic compliance minimization problem of Section 7.1

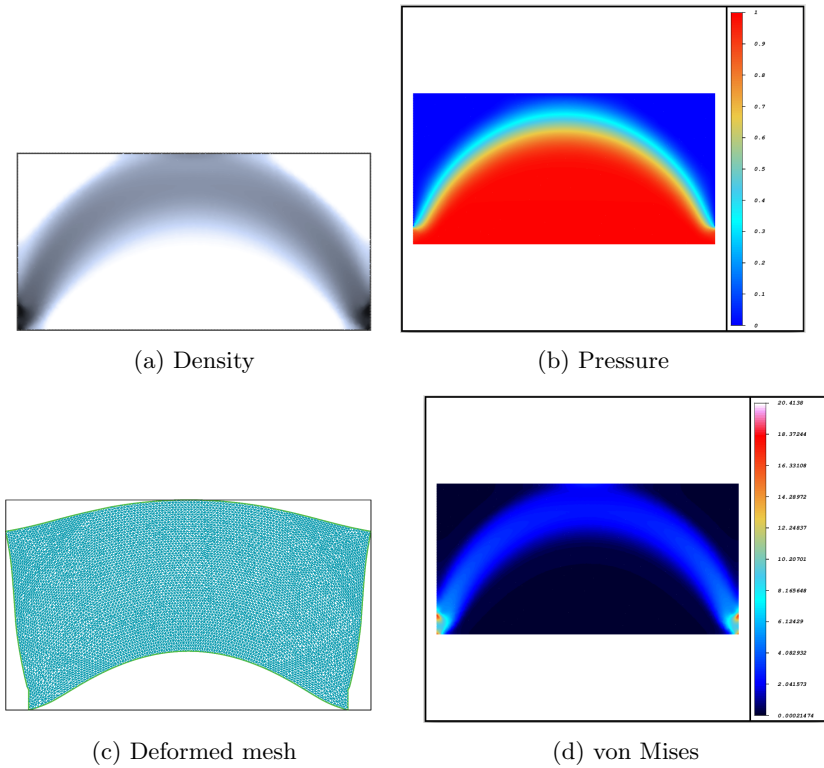


Fig. 8 (a) The optimal density, (b) pressure field, (c) deformed mesh, and (d) von Mises stress for test case 7.1

7.2 Pressurized piston

This second test case was originally introduced and solved in [15, 23]. The workspace is a $0.12m \times 0.04m$ rectangle, fixed on the boundary Γ_D^s , while submitted to pressure load $p = 1$ bar on the upper boundary Γ_p^f and vanishes on boundary $\Gamma_{p_0}^f$; see Fig.9 for a schematic of the test case. The volume fraction is set to $\Theta = 30\%$. It is desired to find a stiffest optimum design "shape" which can convey the applied pressure loads on the upper boundary to the lower fixed support readily.

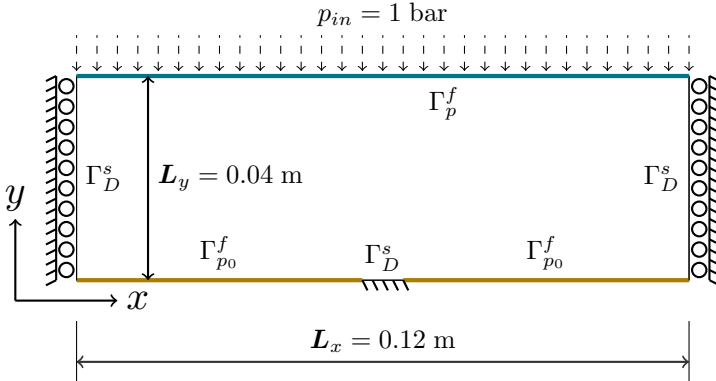


Fig. 9 Setting for fluid-elastic compliance minimization problem of test case 7.1 issued from [15, 23]

On Fig.10, we plot the convergence history for this calculation: smooth and relatively rapid convergence is observed; while Fig.11 depicts the optimal density and the pressure field, deformed mesh, and von Mises stress at final state. The topology of the result is similar to that obtained in previous literature [9, 20, 21, 23], for similar problems with different design and optimization settings. It is noted that, from a relatively diffused initial interface, the boundary exposed to pressure loading is gradually formed during the optimization process. Although one can guess a "shape" on the edges of the structure, its center contains a large composite zone.

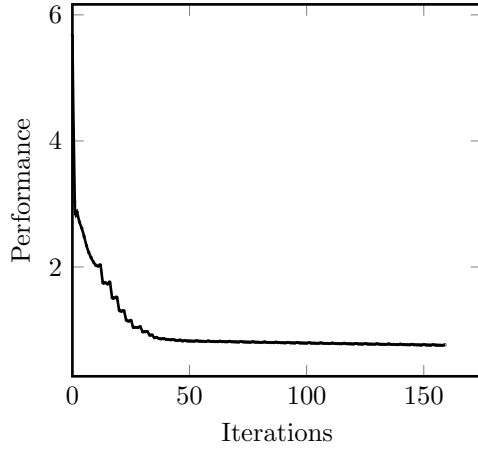


Fig. 10 Convergence history for the fluid-elastic compliance minimization problem of Section 7.2

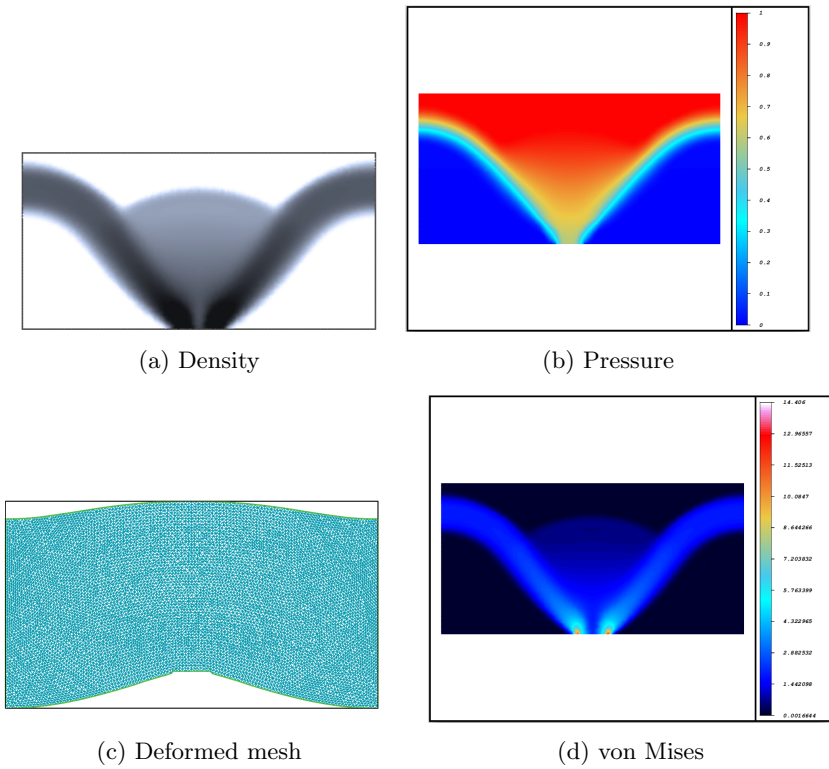


Fig. 11 (a) The optimal density, (b) pressure field, (c) deformed mesh, and (d) von Mises stress for test case 7.2

7.3 Pressurized MBB

In this test case, the structure to be found is submitted to pressure load $p_{in} = 1$ bar on the boundary Γ_p^f , while its boundary Γ_D^s is clamped. The workspace Ω is sketched on Fig.12: a rectangle of dimensions $0.3m \times 0.1m$. The domain is discretized with 43440 triangular elements, where the volume fraction is set to $\Theta = 30\%$. Note that, this example has already been investigated by several authors in the case of structural design under mechanical loading.

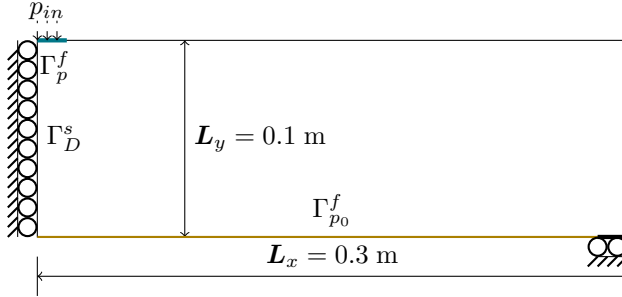


Fig. 12 Setting for fluid-elastic compliance minimization problem of Section 7.3

on Fig.13, we plot the convergence history for this calculation: smooth and relatively fast convergence is observed, while Fig.14 displays the topology of the final design and the resulting von Mises stress, pressure field and deformed mesh under pressure loads at the final state. Very interestingly, we retrieve the fact that the topology of the result is similar to that obtained in the case of mechanical load.

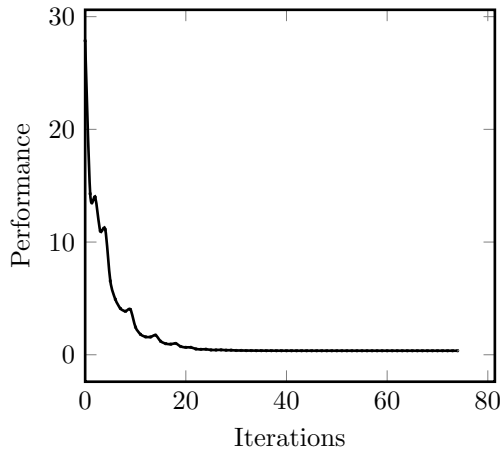


Fig. 13 Convergence history for the fluid-elastic compliance minimization problem of Section 7.3

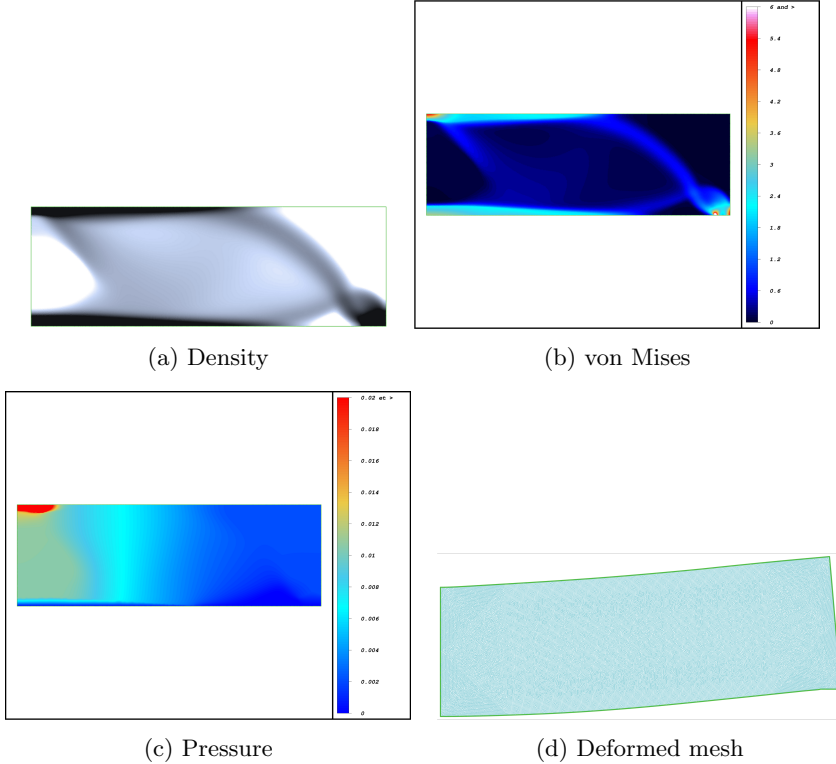


Fig. 14 (a) The optimal density, (b) von Mises stress, (c) pressure field, and (d) deformed mesh for test case 7.3

7.4 Two dimensional counter-flow exchanger

In this example, the structure to be found is a two-dimensional counter-flow exchanger of dimensions 2×2.2 . The setup is seen in Fig.15 and consists of a fluid inlet of density $\mathbf{q}_{0,1}$, in the lower-left part of the domain, with the corresponding outlet pressure on the opposite lower-right side; also, another fluid inlet of density $\mathbf{q}_{0,2}$ is located at the upper-right side of the domain, with the corresponding outlet pressure at the opposite upper-left side. All the other boundaries in this device are insulated from the outside: zero Neumann boundary conditions hold for the pressure (i.e., $\frac{\partial p}{\partial n} = 0$), while homogeneous Dirichlet boundary conditions are applied on the boundary of a small non optimizable rectangle ω of dimensions 2×0.2 . The numerical values of the parameters involved are displayed on Fig.16.

Our aim is to achieve a trade-off between the minimization of the compliance imposed by the fluid and the maximization of the hydraulic strain energy,

subject to the volume constraint (or not), that is:

$$J^*(\theta, u(\theta)) = \underbrace{\alpha \left(\int_{\Omega} A^* e(u) : e(u) dx \right)}_{\text{Elastic strain energy}} + (1 - \alpha) \underbrace{\left(- \int_{\Omega} K^* \nabla p \cdot \nabla p dx \right)}_{\text{Hydraulic strain energy}},$$

$$s.t. \left\{ \frac{1}{|\Omega|} \int_{\Omega} \theta dx = \Theta \right.$$
(68)

where $\alpha \in [0, 1]$ is termed as a weighting factor: it measures the relative weight given to each term in (68). The objective functional $J^*(\theta, u(\theta))$ corresponds to the internal energy stored inside the structure. Here, we consider to two configurations, i.e.: (i) a test case with volume constraint set to $\Theta = 20\%$, first and (ii) test case without volume constraint, second, for several values of α .

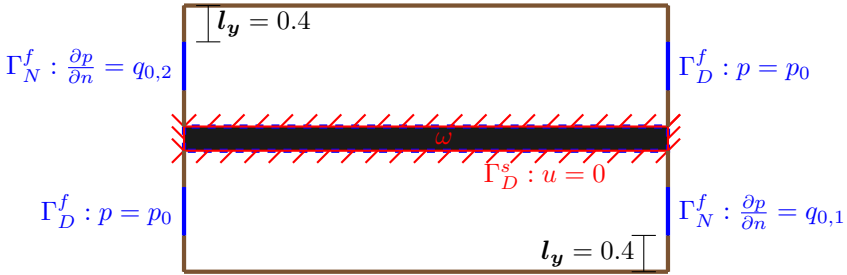


Fig. 15 Setting of the 2-d counter-flow exchanger 7.4. The brown layers at the walls stand for zero Neumann boundary conditions for the pressure (i.e., $\frac{\partial p}{\partial n} = 0$); homogeneous Dirichlet boundary conditions hold on $\partial\omega$.

p_0	$q_{0,1}$	$q_{0,2}$
1.5	3	5

Fig. 16 Numerical values of the physical parameters in the 2-d counter-flow exchanger test case in Section 7.4

Fig. 17 to Fig. 18 display the optimal densities for a sweep of α for the two configurations, i.e.: with or without volume constraint. Very interestingly, we retrieve the fact that the topology of the results contains a large composite zone, where the force contribution induced by the fluid appears in all directions, which evidently, prior to the analysis is expected. For this latter, the corresponding objective history for the two configurations are depicted on Fig. 19 to Fig. 20. On Fig. 21, we plot the final volume with respect to α for the second configuration (i.e., with volume unconstrained), while on Fig. 22 to Fig. 23,

we show the convergence history for $\alpha = 1/2$ for the both configurations. On Fig. 24, we display the corresponding pressure field for both configurations, with $\alpha = 1/2$.

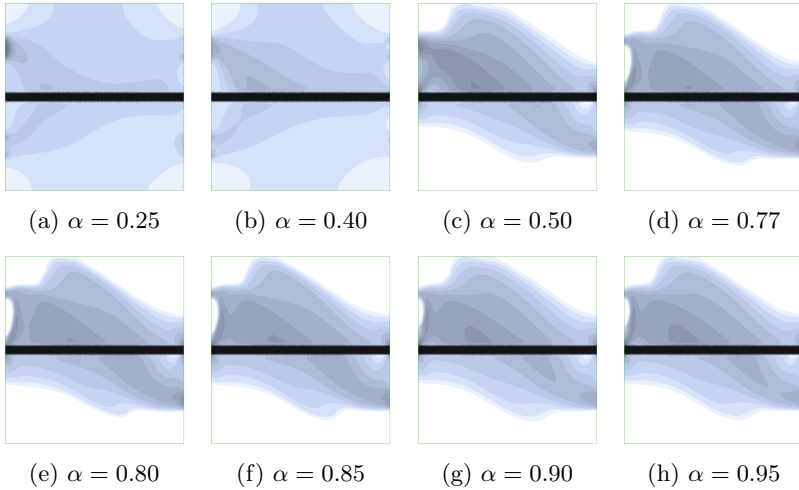


Fig. 17 The Optimal densities for a sweep of α , with volume fraction $\Theta = 20\%$

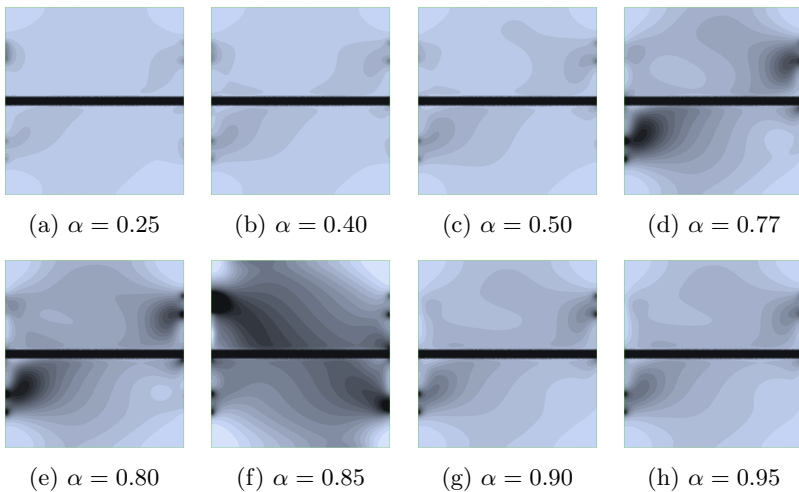


Fig. 18 The Optimal densities for a sweep of α , without volume constraint

α	0.25	0.40	0.50	0.77	0.85	0.90	0.93	0.95
$J^*(\alpha)$	-4.51	-0.06	0.962	5.055	5.025	6.533	10.17	0.163

Fig. 19 The converged objective function wrt. α , with volume fraction $\Theta = 20\%$

α	0.25	0.40	0.50	0.77	0.85	0.90	0.93	0.95
$J^*(\alpha)$	-4.51	-2.54	-1.83	-0.57	-0.55	-1.47	0.026	0.286

Fig. 20 The converged objective function wrt. α , without volume constraint

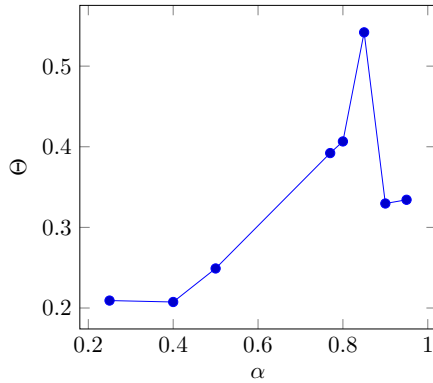


Fig. 21 The final volume history wrt. α , in the second configuration, i.e., without volume constraint.

We note that, in both configurations, namely when the optimization is subjected to a volume constraint or not, the topology of the optimal design is α dependent, namely, for all $\alpha \in (0, 0.40)$, the topology tends to maximize the hydraulic strain energy, which in process minimize the output pressure, whereas for all $\alpha \in [0.40, 1)$, the topology of the result tends to achieve a trade-off between the minimization of the compliance induced by the fluid and the maximization of the hydraulic strain energy, which evidently is what we intent to achieve for this optimization problem. However, in the second configuration (i.e., without volume constraint), we emphasize a gain of volume fraction but not necessarily a gain in performance, see Fig. 20.

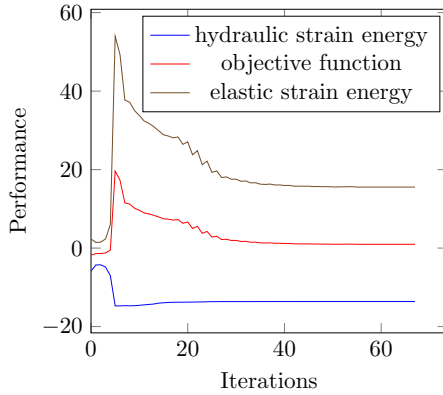


Fig. 22 The convergence history wrt. $\alpha = 1/2$, for volume constraint $\Theta = 20\%$

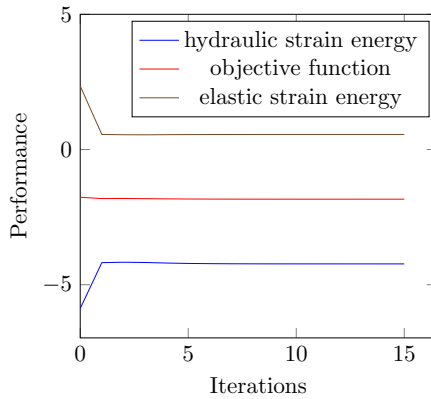


Fig. 23 The convergence history wrt. $\alpha = 1/2$, and with no volume constraint

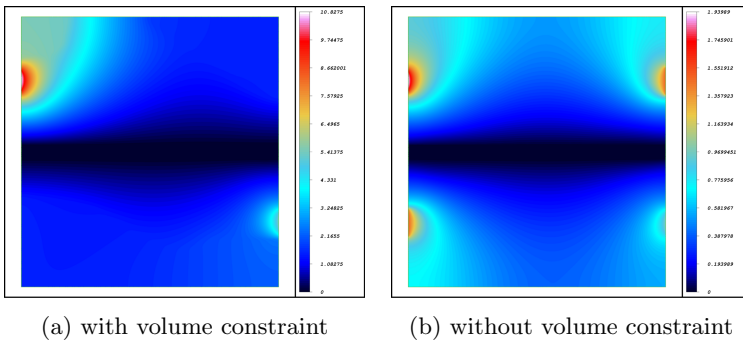


Fig. 24 The pressure field at final state for both configuration: with and without volume constraint, for $\alpha = 1/2$

8 Conclusion and perspectives

In this paper, a novel approach to perform topology optimization of design problems involving fluidic pressure loaded structures was presented using the homogenization method. The approach permits use of standard finite element formulation and does not require explicit boundary description or tracking. As the fluidic pressure loads vary with the shape and location of the exposed structural boundary, a main challenge in such problems is to determine design-dependent pressure field and its design sensitivities. In the proposed method, Biot-Darcy's law is used to define the design dependent pressure field by solving an associated **PDE** using the standard finite element method. The porosity of each **FE** is related to its material density via a smooth enough function to ensure a smooth transition between void and solid elements. The Biot's coefficient is also related to material density, explicitly defined in the case of isotropic porous medium, where the determined pressure field is further used to find the consistent nodal loads. In the early stage of the optimization, the obtained nodal loads are spread out within the design domain and thus, may enhance exploratory characteristics of the formulation and thereby the ability of the optimization process to find well-performing solutions. Furthermore, the Biot-Darcy's parameters, selected a priori to the optimization, affect the topologies of the final density. The method facilitates analytical calculation of the load sensitivities with respect to the design variables using the computationally inexpensive adjoint-variable method. This availability of load sensitivities is an important advantage over various earlier approaches to handle pressure loads in topology optimization. In addition, it is noticed that consideration of load sensitivities within the approach does alter the final density designs, and that the load sensitivities terms are particularly important when designing pressure loaded structures. Moreover, in contrast to methods that use explicit boundary tracking, the proposed Biot-Darcy method offers the potential for relatively straightforward extension to 3D problems. The effectiveness and robustness of the proposed method is verified by minimizing the sum of the elastic and fluid-elastic compliance, and of the weight of a solid structure under pressure loads. The method allows relocation of the fluidic pressure-loaded boundary during optimization, and smooth and steady convergence is observed. Extension to 3D structures and to liquid-liquid heat exchangers problems are prime directions for future research.

Declarations

On behalf of all authors, the corresponding author states that there is no conflict of interest.

Replication of results

On behalf of all authors, the corresponding author states that there is no codes available as supplementary material because this work is carried out as part of a thesis in partnership with IFPEN. The latter holds the intellectual rights.

References

- [1] Hammer, V.B. and Olhoff, N., Topology optimization of continuum structures subjected to pressure loading, *J. Structural and Multidisciplinary Optimization*, 19(2) (2000) 85-92.
- [2] Papazoglou, P., Topology optimization of heat exchangers, TU Delft, (2015).
- [3] Pietropaoli, M. and Montomoli, F. and Gaymann, A., Three-dimensional fluid topology optimization for heat transfer, *J. Structural and Multidisciplinary Optimization*, 59 (2019) 801-812.
- [4] Saltzman, D. and Bichnevicius, M. and Lynch, S. and Simpson, T.W. and Reutzel, E.W. and Dickman, C. and Martukanitz, R., Design and evaluation of an additively manufactured aircraft heat exchanger, *J. Applied Thermal Engineering*, 138 (2018) 254-263.
- [5] Saviers, K.R. and Ranjan, R. and Mahmoudi, R., Design and validation of topology optimized heat exchangers, *AIAA Scitech 2019 Forum*, 1465.
- [6] Feppon, F. and Allaire, G. and Bordeu, F. and Cortial, J. and Dapogny, C., Shape Optimization of a Coupled Thermal Fluid-Structure Problem in a Level Set Mesh Evolution Framework, *J. Boletín de la Sociedad Española de Matemática Aplicada*, Springer 76(3) (2019) 413-458.
- [7] Du, J. and Olhoff, N., Topological optimization of continuum structures with design-dependent surface loading - Part I: New computational approach for 2D problems, *J. Structural and Multidisciplinary Optimization* 27(3) (2004) 151-165.
- [8] Fuchs, M.B. and Shemesh, NNY., Density-based topological design of structures subjected to water pressure using a parametric loading surface, *J. Structural and Multidisciplinary Optimization*, 28(1) (2004) 11-19.

- [9] Lee, E. and Martins, JRRA., Structural topology optimization with design-dependent pressure loads., *J. Computer Methods in Applied Mechanics and Engineering*, 40-48 (2012) 233-236.
- [10] Li, Zm and Yu, J. and Xu, L., N., Topology optimization of pressure structures based on regional contour tracking technology, *J. Structural and Multidisciplinary Optimization*, 58(2) (2018) 687-700.
- [11] Zheng, B. and Chang, C.J. and Gea, H.C., Topology optimization with design-dependent pressure loading, *J. Structural and Multidisciplinary Optimization*, 38(6) (2009) 535-543.
- [12] Gao, X. and Zhao, K. and Gu, Y., Topology optimization with design-dependent loads by level set approach, In: 10th AIAA/ISSMO Multidisciplinary Analysis and Optimization Conference, (2004) 4526.
- [13] Li, C. and Xu, C. and Gui, C. and Fox, M.D., Distance regularized level set evolution and its application to image segmentation, *J. IEEE Transactions on Image Processing*, 19(12) (2010) 3243-3254.
- [14] Xia, Q. and Wang, M.Y. and Shi, T., Topology optimization with pressure load through a level set method, *J. Computer Methods in Applied Mechanics and Engineering*, 283 (2015) 177–195.
- [15] Bourdin, B. and Chambolle, A., Design-dependent loads in topology optimization, *ESAIM: Control, Optimisation and Calculus of Variations.*, 9 (2003) 19-48.
- [16] Paganiban, H. and Jang, G.W. and Chung, T.J., Topology optimization of pressure-actuated compliant mechanisms, *ESAIM: Control, Optimisation and Calculus of Variations.*, 46(3) (2010) 238-246
- [17] Sigmund, O. and Clausen, P.M., Topology optimization using a mixed formulation: An alternative way to solve pressure load problems, *J. Computer Methods in Applied Mechanics and Engineering*, 196 (13-16) (2007) 1874-1889.
- [18] Vasista, S. and Tong, L., Design and testing of pressurized cellular planar morphing structures, *AIAA journal*, 50(6) (2012) 1328-1338.
- [19] Zhang, H. and Zhang, X. and Liu, S.T., A new boundary search scheme for topology optimization of continuum structures with design-dependent loads, *J. Structural and Multidisciplinary Optimization*, 37(2) (2008) 121-129.
- [20] Wang, C. and Zhao, M. and Ge, T., Structural topology optimization with design-dependent pressure loads., *J. Structural and Multidisciplinary*

Optimization, 53(5) (2016) 1005-1018.

- [21] Picelli, R. and Neofytou, A. and Kim, H.A., Structural topology optimization with design-dependent pressure loads., *Topology optimization for design-dependent hydrostatic pressure loading via the level-set method*, 60(4) (2019) 1313-1326.
- [22] Zienkiewicz, O.C. and Taylor, R.L., *The Finite Element Method for Solid and Structural Mechanics*, Butterworth-heinemann, 2005.
- [23] Kumar, P. and Frouws, J.S. and Langelaar, M., *Topology Optimization of Fluidic Pressure Loaded Structures and Compliant Mechanisms using the Darcy Method*, Springer: Structural and Multidisciplinary Optimization, 61 (2020) 1637-1655.
- [24] Hübner, D. and Rohan, E. and Lukeš, V. and Stingl, M., Optimization of the porous material described by the Biot model, Elsevier, *International Journal of Solids and Structures*, 156-157 (2019) 216-233.
- [25] Allaire, G. and Bonnetier, E. and Francfort, G. and Jouve, F., Shape optimization by homogenization method, Springer-Verlag. *J. Numer. Math.*, 76 (1997) 27-68.
- [26] Murat, F., Contre-exemples pour divers problèmes où le contrôle intervient dans les coefficients, *Ann. Mat. Pura Appl.*, 112 (1997) 49-68.
- [27] Pantz, O. and Trabelsi, K., A post-treatment of the homogenization method for shape optimization, *SIAM Journal on Control and Optimization*, 47(3) (2008) 1380-1398.
- [28] Geoffrey-Donders, P., Homogenization method for topology optimization of structures built with lattice materials, PhD thesis, Université Paris Saclay (COMUE), 2018.
- [29] Jobic, Y. and Kumar, P. and Topin, F. and Occelli, R., Transport properties of solid foams having circular strut cross section using pore scale numerical simulations, *Heat Mass Transfer*, 54 (2018) 2351-2370.
- [30] Batchelor, G., *An introduction to fluid dynamics*, Cambridge university press, 2000.
- [31] Neuber, H., Theory of notch stresses: principles for exact calculation of strength with reference to structural form and material, USAEC Office of Technical Information, (1961) 4547.
- [32] Abad, K.M.E. and Khanoki, A.S. and Pasini, D.F., Fatigue design of lattice materials via computational mechanics: Application to lattices with

- smooth transitions in cell geometry, *International Journal of Fatigue*, 47 (2013) 126-136.
- [33] Vigdergauz, S., Energy-minimizing inclusions in a planar elastic structure with macroisotropy, *Structural optimization*, 17(2-3) (2013) 104-112.
- [34] Allaire, G., *Shape Optimization by the Homogenization Method*, Springer, Applied Mathematical Sciences, 146 (2002).
- [35] Hashin, Z. and Shtrikman, S., A variational approach to the theory of the elastic behaviour of multiphase materials, *Journal of the Mechanics and Physics of Solids*, 11(2) (1963) 127-140.
- [36] Allaire, G., *Conception optimale de structures*, Springer-Verlag Berlin Heidelberg, Applied Mathematical Sciences, 19(2) (2000) 58 (2007).
- [37] Bendsoe, M. and Diaz, A. and Kikuchi, N., Topology and generalized layout optimization of structures, In: *Topology Optimization of Structures*, Nato ASI Series E, Bendsoe M., et al. (eds), (Kluwer, Dordrecht, 1993) 159-205.
- [38] Jog, C. and Haber, R. and Bendsoe, M., A displacement-based topology design method with self-adaptive layered materials. In: *Topology design of structures*, Nato ASI Series E, Bendsoe M., et al. (eds), *Int. Journal for Numerical Methods in Engineering*, (Kluwer, Dordrecht , 1993) 219-238.
- [39] Jog, C. and Haber, R. and Bendsoe, M., Topology design with optimized, self-adaptative materials, *Int. Journal for Numerical Methods in Engineering*, 39(10) (2003) 1667-1694.
- [40] Bendsoe, M.P. and Kikuchi, N., Generating optimal topologies in structural design using a homogenization method, *Comput. Methods Appl. Mech. Engrg*, 71(2) (1988) 197-224.
- [41] Allaire, G. and Kohn, R.V., Optimal design for minimum weight and compliance in plane stress using extremal microstructures, *Europ. J. Mech. A/Solids*, 12(6) (1993) 839-878.
- [42] Suzuki, K. and Kikuchi, N., A homogenization method for shape and topology optimization, *Comp. Meth. Appl. Mech. Eng.*, 93 (1991) 291-318.
- [43] Hecht, F., *J. Math. Anal. Appl.*, New development in freefem++, *J. Numerical Mathematics*, (2012).
- [44] Chen, B.C. and Kikuchi, N., Topology optimization with design-dependent loads. *Finite elements in analysis and design*, *ESAIM: Control, Optimisation and Calculus of Variations.*, 37(1) (2001) 57-70.